Geomorphological and hydrological controls on sediment export in earthquake-affected catchments in the Nepal Himalaya

Emma L. S. Graf[1], Hugh D. Sinclair[1], Mikaël Attal[1], Boris Gailleton[2], Basanta Raj Adhikari[3], and Bishnu Raj Baral[4]

[1]School of GeoSciences, University of Edinburgh, Edinburgh, UK
[2]Geosciences Rennes, University of Rennes 1, Rennes, France
[3]Institute of Engineering, Tribhuvan University, Kathmandu, Nepal
[4]Clean Energy Consultant Pvt. Ltd., Kathmandu, Nepal

Correspondence: Hugh Sinclair (hugh.sinclair@ed.ac.uk)

Abstract. Large earthquakes can contribute to mountain growth by building topography, but also contribute to mass removal from mountain ranges through widespread mass wasting. On annual to decadal timescales, large earthquakes also have the potential to significantly alter fluvial sediment dynamics if a significant volume of the sediment generated reaches the fluvial network. In this contribution, we focus on the Melamchi-Indrawati and Bhote Koshi rivers in central Nepal, which have both

5 experienced widespread landsliding associated with the 2015 Gorkha (Nepal) earthquake. Using a time series of high-resolution satellite imagery, we have mapped exposed gravel along the river from 2012-2021 to identify zones of active channel deposition and document changes over time. Counter to expectations, we show negligible increases in coarse sediment accumulation in both catchments since the Gorkha earthquake. However, an extremely high concentration flow event on 15 June 2021 caused an approximately four-fold increase in exposed gravel along a 30 km reach of the channel with up to 12 m of channel aggradation

10 in the Melamchi-Indrawati rivers; this event was localised and did not impact the neighbouring Bhote Koshi catchment. Based on published reports, new helicopter based photography and satellite data, we demonstrate that this event was sourced from a localised rainfall event between 4500 and 4800 m, and that the majority of the sediment was supplied from sources that were unrelated to the landslides generated by the Gorkha earthquake.

1 Introduction

15 By building topography, large earthquakes contribute to the growth of mountain ranges (Avouac, 2007), but they also play a role in their erosion by producing sediment through coseismic landsliding, which will eventually be evacuated from the mountain range (e.g. Keefer, 1994; Dadson et al., 2004; Larsen et al., 2010; Hovius et al., 2011; Parker et al., 2011; Egholm et al., 2013). In some cases, the volume lost through mass wasting can equal or even outweigh that gained through surface uplift (e.g. Hovius et al., 2011; Parker et al., 2011; Marc et al., 2016, 2019; Francis et al., 2020). Malamud et al. (2004) suggest that earthquakes above a threshold moment magnitude of $M_w = 4.3$ trigger landslides through ground shaking, with landslides usually concentrated in areas of highest peak ground acceleration (PGA) (Khazai and Sitar, 2004) and near the top of hillslopes (Densmore and Hovius, 2000; Yin et al., 2009). The sediment generated by coseismic landsliding either remains

on the hillslopes or is delivered to fluvial systems, where it can cause aggradation and decrease channel capacity, thereby
increasing flood risk downstream and causing rapid changes in channel morphology (Korup et al., 2004; Sims and Rutherfurd,
25 2017). For example, the 1999 Chi-Chi (Taiwan) and 2008 Wenchuan (China) earthquakes were associated with up to 18 m
and 10 m of channel bed aggradation, respectively (Chen and Petley, 2005; Whadcoat, 2011; Yanites et al., 2010). Coseismic
landslide sediment on hillslopes often remains as loose sediment until hillslopes re-vegetate or re-stabilise, which may take
years. Consequently, large earthquakes are frequently followed by a period of increased landsliding as the ground shaking
destabilises hillslope material, leaving loose sediment readily mobilised during subsequent rainfall events (Dadson et al., 2004;
30 Chen and Petley, 2005; Huang and Fan, 2013; Marc et al., 2015). In the two years following the Kashmir earthquake, Saba
et al. (2010) documented an increase in landsliding, succeeded by a period of relative stability, while Li et al. (2022) show a
growth in landslide area for five years after the 2008 Wenchuan earthquake. Similarly, Kincey et al. (2021) noted elevated rates
of landsliding for three years in the wake of the 2015 Gorkha earthquake.

Coseismic landslides are thought to affect the fluvial network for decades to centuries (Croissant et al., 2017; Hovius et al.,
35 2011; Wang et al., 2015; Yanites et al., 2010; Wang et al., 2017). Wang et al. (2015) estimate that the residence time of
suspended sediment supplied by coseismic Wenchuan landslides ranges from a year to more than a century, which ties in with
previous estimates of sub-annual to centennial timescales, as suggested by a range of studies from across the globe (Pain and
Bowler, 1973; Pearce and Watson, 1986; Koi et al., 2008; Howarth et al., 2012). The residence time of coseismic bedload
is more challenging to constrain due to the difficulty of monitoring bedload transport (Li et al., 2014; Croissant et al., 2017),
40 although based on a case study of a large landslide in the Bhote Koshi valley, Croissant et al. (2017) estimate that half the coarse
fraction of a given sediment volume can be removed within 5-25 years by channel narrowing to increase sediment transport
capacity.

Our study focuses on the Melamchi-Indrawati and Bhote Koshi valleys in central Nepal that were both affected by the 2015
Gorkha earthquake. The earthquake had a similar moment magnitude to the 2008 Wenchuan earthquake (M_w 7.8 compared
45 to M_w 7.9) and caused widespread landsliding (e.g. Collins and Jibson, 2015; Gnyawali and Adhikari, 2017a; Roback et al.,
2018). Here, we use optical satellite imagery to identify zones of sediment input and aggradation along the Melamchi-Indrawati
and Bhote Koshi rivers. Our analysis focuses on the period 2012-2021 which includes the Gorkha earthquake, as well as a
series of major hydrological events such as the 2021 Melamchi flood, which will be presented below. The aim of this work
is to constrain the respective roles played by the earthquake, valley morphology and major hydrological events on sediment
50 production and export. In particular, we will assess the extent to which the Melamchi flood event was pre-conditioned by
increased sediment availability following the Gorkha earthquake, using photographic evidence from reconnaissance helicopter
flights and initial publications.

2 The 25 April 2015 M_w 7.8 Gorkha (Nepal) earthquake and associated landslides

The April 2015 Gorkha earthquake was the result of a 140 km long rupture along the Main Himalayan Thrust (Avouac et al.,
55 2015; Hayes et al., 2015; Elliott et al., 2016). A sequence of aftershocks followed the main event, the largest of which occurred

on 12 May 2015 in the Dolakha district of Nepal (Fig. 1), reaching a moment magnitude of 7.3 (Collins and Jibson, 2015). Nine thousand deaths and billions of US dollars in economic losses resulted from the mainshock alone (Kargel et al., 2015). While initial surveys (e.g. Kargel et al., 2015) reported a significantly lower number of landslides than expected for an earthquake of moment magnitude 7.8, later inventories identified up to 25,000 coseismic landslides covering a total area of ca. 87 km^2

60 (Martha et al., 2017; Roback et al., 2018), which is more consistent with expectations (Malamud et al., 2004). Most landslides observed in the months following the earthquake had been initiated in weathered and fractured surface material (Collins and Jibson, 2015). In terms of regional landslide distribution, Roback et al. (2018) report no regional lithological control – instead, landslides are concentrated where high peak ground acceleration (PGA), steep slopes and high mean annual precipitation coincide. Regarding landslide threat to human populations, Collins and Jibson (2015) documented over 69 partial, full or

65 temporary landslide dams in the aftermath of the earthquake, although formation of a landslide lake was observed for only half the dams. At the time of writing, a wide range of Gorkha landslide inventories have been published, mapping coseismic landslides as points (Kargel et al., 2016; Tiwari et al., 2017), a mixture of points, polygons and polylines (Robinson et al., 2017; Williams et al., 2018), or polygons (Regmi et al., 2016; Gnyawali and Adhikari, 2017a; Martha et al., 2017; Roback et al., 2018; Xu, 2018; Kincey et al., 2021; Valagussa et al., 2021). Of these inventories, Roback et al. (2018) appears the most

70 complete, including 24,915 landslides covering a total area of 87 km^2 and separating the full landslide area from the landslide source.

3   Study area

Our study focuses on the Melamchi-Indrawati and Bhote Koshi catchments. Both are located in Nepal's Sindhupalchok district, which was one of the worst affected areas in the aftermath of the Gorkha earthquake in terms of landslide density (e.g. Collins

75 and Jibson, 2015; Kargel et al., 2016; Roback et al., 2018). Of the 87 km^2 of landslides triggered by the Gorkha earthquake and mapped by Roback et al. (2018), 12.3 km^2 are located in the Melamchi-Indrawati catchment and 24.5 km^2 in the Bhote Koshi (Roback et al., 2018). Here, we explore how these mountain catchments react to large-scale input of coseismic landslide sediment.

80   The Melamchi-Indrawati catchment is located ca. 20 km east of Kathmandu (Fig. 1) and the Indrawati River is fed by three main tributaries, the Melamchi, Yangri, and Larke rivers (Fig. 1b), originating in the Kanja La range. We focus on the Melamchi River and the Indrawati River downstream of its confluence with the Melamchi River, herein referred to as the Melamchi-Indrawati rivers. Elevations in the Indrawati catchment range from around 600 m at Dolalghat to >5000 m, and the climate spans temperate to polar tundra environments (Pandey et al., 2021). Above Nakote, the Melamchi River is steep and

85 narrow, confined into a "classic" V-shaped valley; it widens downstream of Nakote to include fertile agricultural land on its banks (Baskota et al., 2021) (Fig. 1b). Downstream of Melamchi Bazaar, the Indrawati River widens into a braided system with a floodplain reaching up to a kilometre in width. The catchment also hosts the Melamchi Water Supply Project, currently under construction, aiming to supply water to households as far away as Kathmandu (e.g. Rest, 2019).

The Bhote Koshi, called Poiqu in China, originates in China's Nyalam County (Liu et al., 2020). At 3400 km^2, its catchment
is almost three times the size of the Melamchi-Indrawati and sources roughly half of its area from the Tibetan Plateau (Fig. 1c).
As in the Melamchi-Indrawati, the climate in the Bhote Koshi catchment ranges from temperate to polar (Karki et al., 2016),
and the lower, temperate part of the catchment features distinct wet and dry seasons, with ∼80% of the annual precipitation
occurring during the Indian Summer Monsoon (Bookhagen and Burbank, 2010). Annual rainfall is high, ranging between 1300
and 4100 mm (Tanoli et al., 2017), and the Bhote Koshi is prone to glacial lake outburst floods (GLOFs) – Khanal et al. (2015)
reported six GLOFs in the Bhote Koshi since 1935. The Araniko Highway, an important trade and transport route and one of
the two routes linking Nepal with China (Liu et al., 2020; Whitworth et al., 2020), runs alongside the Bhote Koshi.

3.1 Geologic and geomorphic setting

Both the Melamchi-Indrawati and Bhote Koshi catchments lie within the gneisses, schists, quartzites and Miocene granitic
intrusions of the Higher Himalayan Crystallines (HHC) and the lower-grade metamorphic rocks (phyllites, quartzites, and
slates) of the Lesser Himalayan Sequence (LHS), which are separated by the Main Central Thrust (MCT) (Gansser, 1964;
Upreti, 1999; Department of Mines and Geology, 2011). The Bhote Koshi catchment additionally extends into the carbonate-
dominated sedimentary rocks of the Tethyan Himalayan Sequence, separated from the HHC by the South Tibetan Detachment
(STD) (Yin, 2006), as shown in Fig. 1a. Our studied reach along the Melamchi-Indrawati rivers (Fig. 1b) extends through the
HHC, crosses the MCT, and then flows predominantly through LHS units, including the quartzites of the Syangja Formation,
as well as the Seti Formation's phyllites and quartzites (Department of Mines and Geology, 2011). The Bhote Koshi study
reach (Fig. 1c) lies mostly within the LHS, predominantly the phyllites and quartzites of the Seti Formation, and also flows
through LHS shales, slates and limestones in the MCT zone near the Nepal-China border (Department of Mines and Geology,
2011).
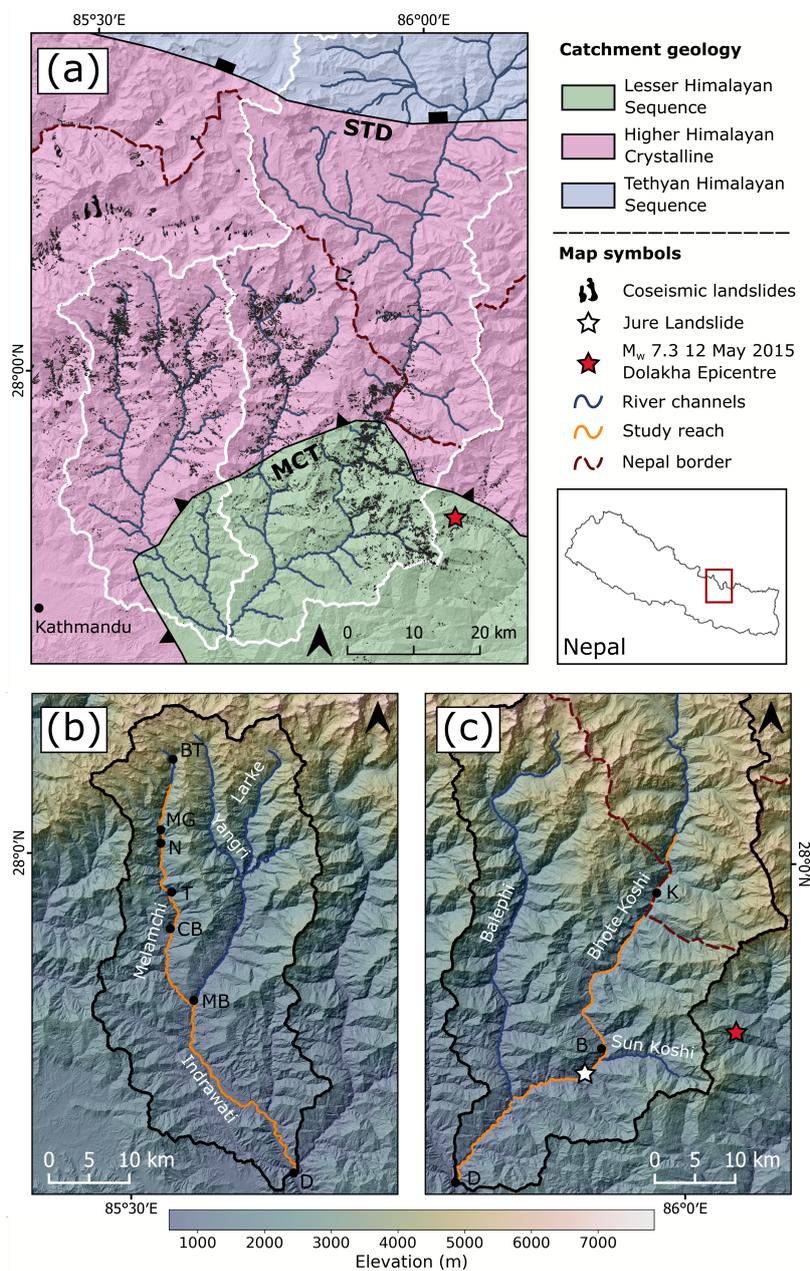
Figure 1. (a) Catchment geology adapted from Yin (2006) and Dhital (2015). Gorkha landslides mapped by Roback et al. (2018) shown as black polygons. The two studied catchments are delineated by the white outline: Melamchi-Indrawati to the west and Bhote Koshi to the east. (b) Melamchi-Indrawati catchment with main rivers and localities mentioned in text labelled. (c) Bhote Koshi catchment with main rivers and localities mentioned in text labelled. Studied river reaches are shown in orange. Background of all three panels is a shaded relief map from a 30 m Copernicus DEM. B = Bahrabise, BT = Bremthang, CB = Chanaute Bazaar, D = Dolalghat, K = Kodari, MB = Melamchi Bazaar, MG = Melamchigaon, N = Nakote, T = Timbu; MCT = Main Central Thrust, STD = South Tibetan Detachment.

3.2 Significant hydro-geomorphic events

110 This section briefly presents significant hydro-geomorphic events in both catchments which occurred in the time frame covered by our study (2012-2021).

In August 2014, collapse of the hillside at Jure village along the Bhote Koshi produced 6 million m^3 of debris, killing 156 people and creating a deposit 100 m thick that also reached the opposite bank of the river (van der Geest, 2018). The landslide created a 55 m high dam blocking the river and forming a 3 km long lake which filled and overflowed in 12 hours (Acharya

115 et al., 2016). The landslide dam eventually breached on 7 September, mostly due to overtopping (Lamichhane et al., 2021). According to van der Geest (2018), the landslide was triggered by heavy rainfall during the preceding two days; the slope had been noted as unstable in the years before the event (Shrestha and Nakagawa, 2016; Ao et al., 2020).

Originating from Gongbatongshacuo Lake in Tibet Autonomous Region, China, a moraine-dammed lake which broke its dam as a result of a rainfall-induced debris flow, a GLOF swept along the Bhote Koshi on 5 July 2016 (Cook et al., 2018),

120 destroying or damaging parts of the Araniko highway, buildings in Kodari and Tatopani, and the intake dam of a hydropower project.

Four years later, on 9 July 2020, heavy monsoon rainfall caused a debris flow along the Bhote Koshi which killed two people, destroyed or damaged dozens of houses, swept away a 700 m stretch of the Araniko Highway, and damaged the Middle Bhotekoshi Hydropower Project (Lamichhane et al., 2021).

125 Along the Melamchi River, a flash flood occurred on 15 June 2021, lasting for ten hours, and depositing up to 12 m of mostly sand and silt in the river channel (Fig. 2) (Pandey et al., 2021). Five people were killed, with 20 still missing as of September 2021, and 525 families were displaced by the event. The flood damaged 337 houses, severely damaged the headworks of the Melamchi Water Supply Project, delaying delivery of water to households in Kathmandu, and disrupted access to several villages by blocking roads and damaging or destroying more than a dozen bridges (Baskota et al., 2021; Maharjan et al.,

130 2021; Pandey et al., 2021). Maharjan et al. (2021) report that within the Melamchi Municipality alone, more than 1.75 km^2 of agricultural land, crucial for subsistence farming, were lost in the wake of the event. The event is thought to have been caused by a combination of glacial moraine collapse, landslide dam outburst and heavy precipitation (Baskota et al., 2021; Maharjan et al., 2021). On 31 July 2021, a second debris flow scoured the area previously devastated by the prior event (Baskota et al., 2021). The exact source of sediment for this event is explored further below.

135 The above events are well constrained in space and time, facilitating taking into account their impact during interpretation of our data.
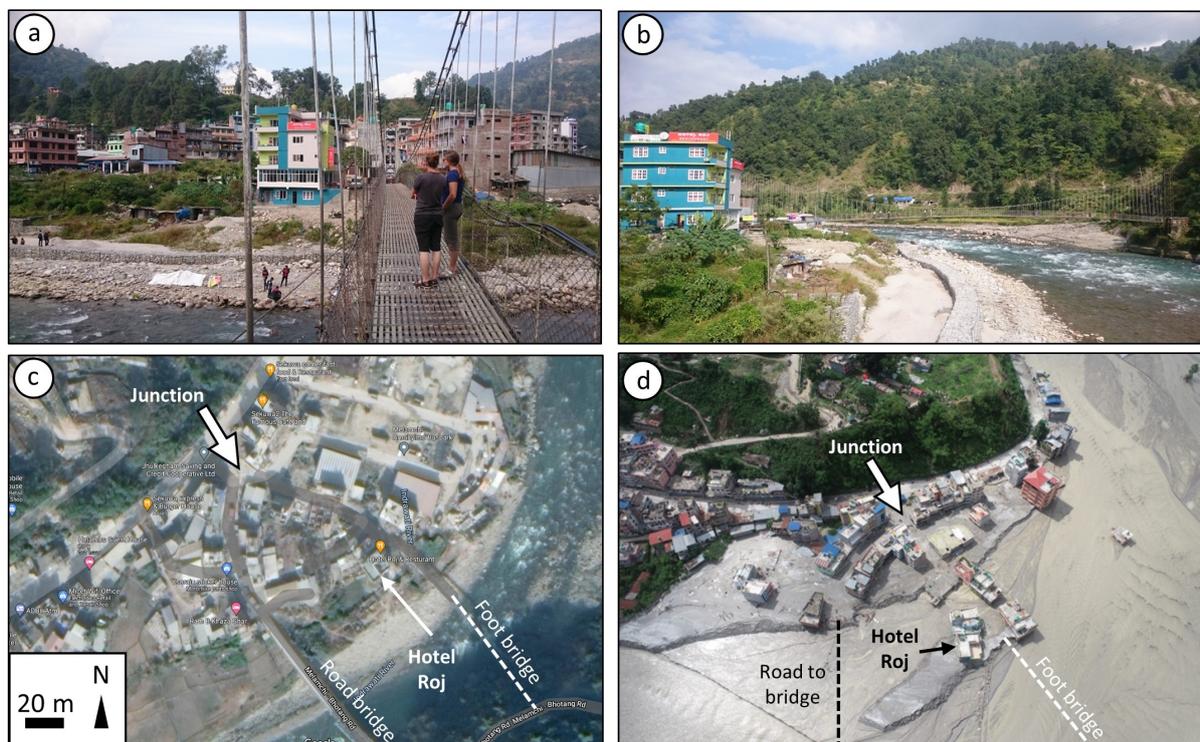
Figure 2. Impact of the 2021 Melamchi flood in Melamchi Bazaar. (a) Picture from footbridge towards Melamchi Bazaar, looking NW, taken on 28/10/2019. Colourful building in the centre of the photo is Hotel Roj, used as a reference in the other photos (position: 27.82917, 85.57714). Note gabions along the gravel bar to limit bank erosion during monsoon floods. (b) Picture from road bridge looking NE, upstream the Indrawati River, taken on 28/10/2019. Hotel Roj is to the left. Note gabions on the gravel bar. (c) © Google Map of Melamchi Bazaar before the 2021 Melamchi flood (©2021 Maxar Technologies). Road and foot bridges are located, as well as road junction and Hotel Roj, for reference. (d) Aerial image of Melamchi Bazaar after the main flood event of June 2021, looking NW (source: Geovation Nepal). Both bridges have been destroyed, and only the top two floors of Hotel Roj emerge from the sediment, indicating aggradation in excess of 10 m.

4 Methods

In order to quantify changes in sediment deposition patterns, which could then be linked to events supplying or evacuating sediment and valley morphology, we map exposed gravel along the Melamchi-Indrawati and Bhote Koshi rivers over a time

140 period spanning ten years (2012-2021); these data identify zones of sediment input and quantify planform changes in channel morphology. We then calculate the connectivity of the coseismic landslides triggered by the 2015 Gorkha (Nepal) earthquake to the river network. We measure channel steepness through long river profile analysis and valley width along the study reaches, and we assess their relation to connectivity. Lastly, in light of the significant impact of the 2021 Melamchi event on the morphology of the Melamchi-Indrawati River, we further use optical satellite data and photographic images to identify the

145 sources of sediment for the Melamchi flash floods.

4.1 Determining gravel area along the river channel

4.1.1 Mapping and data processing

We manually mapped exposed gravel along the Melamchi-Indrawati and Bhote Koshi rivers every year from 2012-2021 to document changes after each monsoon. We used sub-metre resolution imagery from Maxar Technologies and CNES/Airbus, available in Google Earth Pro, for the time period between 2012 and 2019 inclusive, and 3 m resolution Planetscope imagery, obtained through Planet's Education and Research Program, for 2020 onward (see Appendix A for the full breakdown of imagery dates and sources). From 2012-2019 inclusive, each river was mapped once per year so that eight post-monsoon mapping epochs were available. For 2020 and 2021, when sufficient imagery was not available in Google Earth Pro, we switched to Planetscope imagery. In 2021, we took advantage of Planetscope's higher temporal resolution to map both rivers monthly from June-December inclusive. In the Melamchi-Indrawati catchment, mapping was carried out from the confluence with the Bhote Koshi at Dolalghat up to 3.5 km upstream of Nakote (Fig. 1b). Along the Bhote Koshi, we mapped from the confluence with the Indrawati at Dolalghat to 10 km upstream of the Nepal-China border crossing at Kodari (Fig. 1c). As it was not possible to pick images from the same month or season every year, we mapped exposed sediment and water combined to avoid changes in exposed gravel area due to seasonal water level variations (Fig. 3).
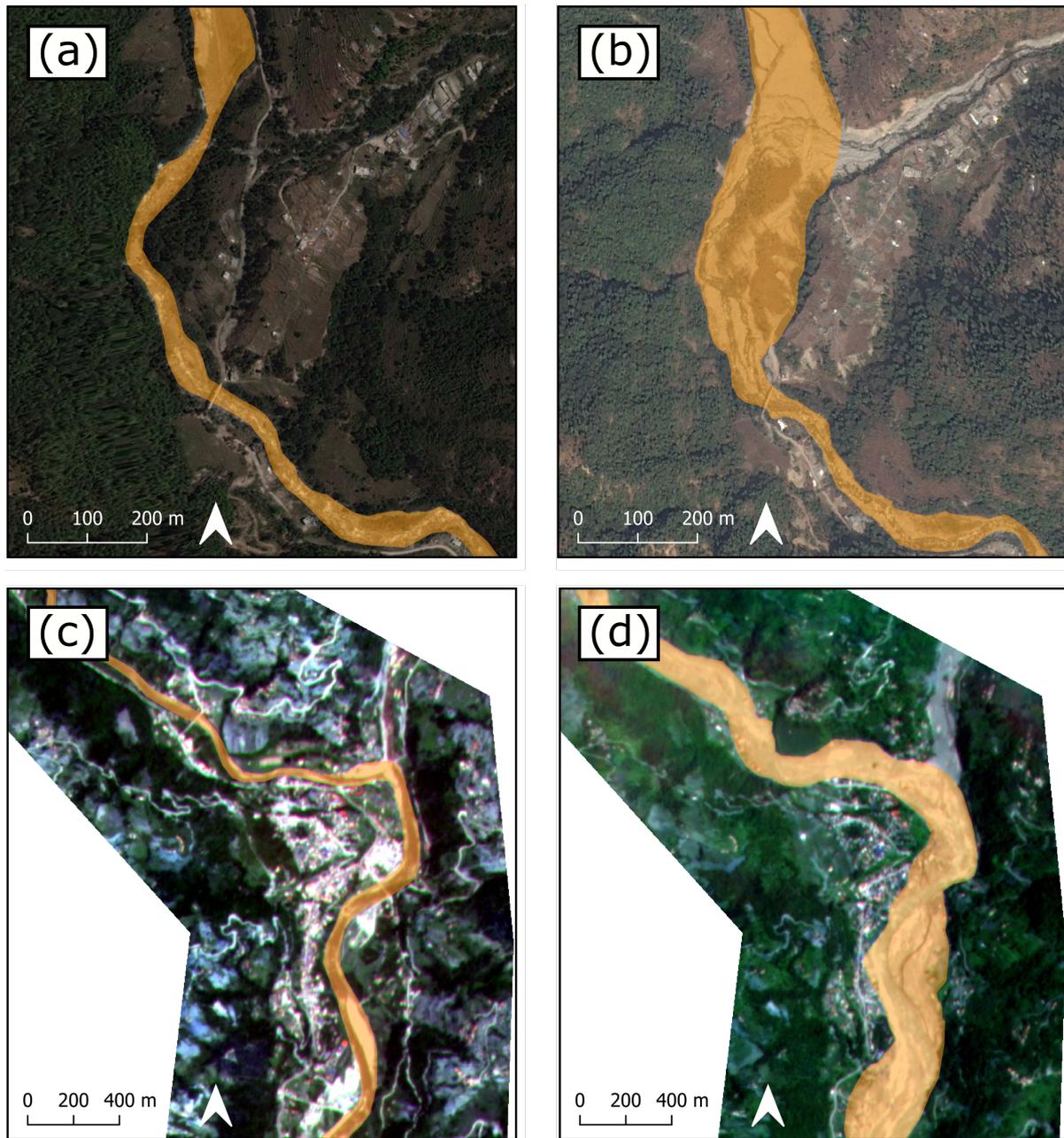
Figure 3. Examples of mapped sections, with the mapped gravel area polygons shown in yellow. Top panels show a section around Timbu overlain on imagery obtained through © Google Earth Pro (©2022 Maxar Technologies). Bottom panels show a section around Melamchi Bazaar overlain on Planetscope imagery (Planet Team, 2017). See Fig. 1b for location of the sections within Melamchi-Indrawati catchment. (a) Gravel area on 3 May 2015; (b) Gravel area on 1 February 2016. Note the influx of gravel from the tributary to the NE; (c) Gravel area on 2 June 2021; (d) Gravel area on 29 July 2021. Note the dramatic increase in gravel area extent following the 15 June 2021 Melamchi disaster.

160   Total area from each mapping epoch is delineated as a single polygon shapefile. In order to calculate and visualise changes in gravel area along the river profile and thereby pinpoint the location of any observed changes, the data are processed as follows (Fig. 4):

1. Each polygon shapefile of gravel area is converted into a raster of a resolution res_r = 40 m.

2. For each river, a polyline shapefile representing the river channel within the studied reach is manually delineated. This
165   polyline is not intended to represent the actual centreline of the river as it is only used to segment the river longitudinally. This polyline shapefile is then split into points with a spacing d_s = 50 m.

3. A window of dimensions d_p x d_o is created centred on each of the points, with d_p representing the window distance along the channel and d_o the window distance orthogonal to the channel. We set d_p = 500 m and d_o = 1000 m in the following. The sensitivity of the results to changing the size of these windows is explored in Appendix A2.

170   4. The area of the raster representing the mapped combined channel area is calculated within each window.

5. This "windowed area" is then plotted against distance along the channel, additionally smoothed using a rolling mean. In the following, we chose a window size k = 7 which achieves the best balance in terms of providing reach-scale information while limiting noise (see sensitivity analysis in Appendix A2).
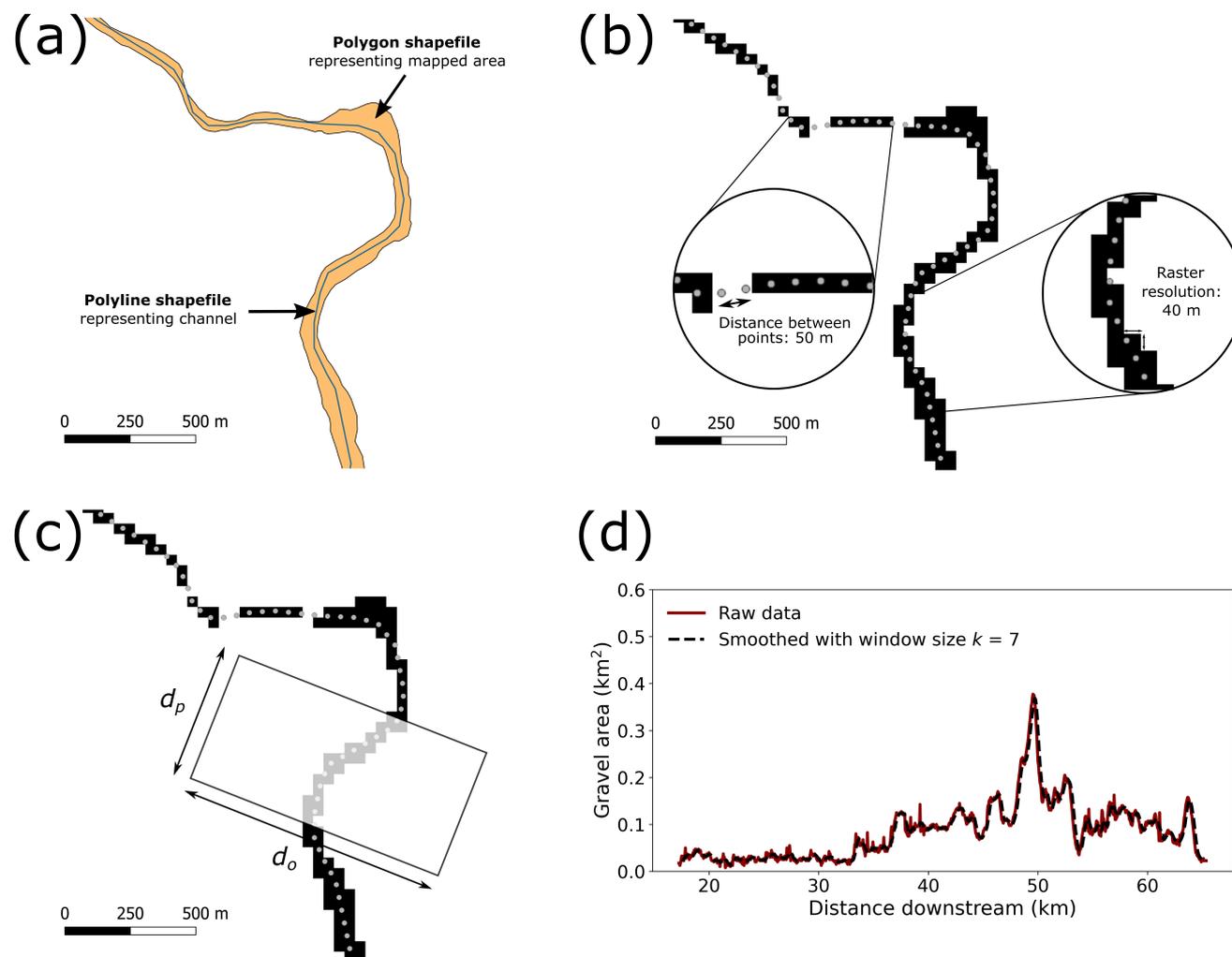
Figure 4. Steps for processing the data shown using an example section near Melamchi Bazaar (see Figs. 1b and 3c, d for location). (a) Original mapped channel and gravel areas. (b) The polygon representing the gravel area is converted to a raster and the line representing the channel is split into points. Note that the rasterisation process creates apparent gaps where gravel areas are narrower than the resolution of the raster res_r; this does not affect the trends in area along the channel (Figs. A1a and A2a in the Supplementary Information). (c) A window of width d_o and length d_p is created around each channel point and the raster area within each window is calculated. (d) The raster area calculated within each window along the river is smoothed using a rolling window and plotted as a function of distance along the channel.

4.1.2 Constraining uncertainty in mapping

175   All the mapping was carried out by one researcher. The rigorous uncertainty calculations following Fan et al. (2018), who had five independent mappers and assessed the degree of matching between each of the five data sets and a reference mapping data set, could therefore not be applied here. Instead, we selected dates on which imagery was available from both Planetscope

and Google Earth Pro, and mapped the full study reach of each image five times, i.e. ten times in total for each river. For the Melamchi-Indrawati rivers, 22 April 2018 was selected, and for the Bhote Koshi, we chose 7/9 December 2017 and 10

180   December 2017 for Google Earth Pro and Planetscope, respectively. Each of the repeatedly mapped areas was then processed as outlined in Section 4.1.1, and the median and standard deviation of the ten mapped area values calculated along each point along the river (Fig. 5). The 75th percentile of the collection of standard deviations was subsequently added as an uncertainty envelope in all plots showing area along profile, and also carried forwards to plots showing expansion/removal of sediment along the profile (Figs. 6 and 7). The uncertainty values are 6.2 x 10^{-3} km^2 for the Melamchi-Indrawati rivers and 5.3 x 10^{-3}

185   km^2 for the Bhote Koshi.
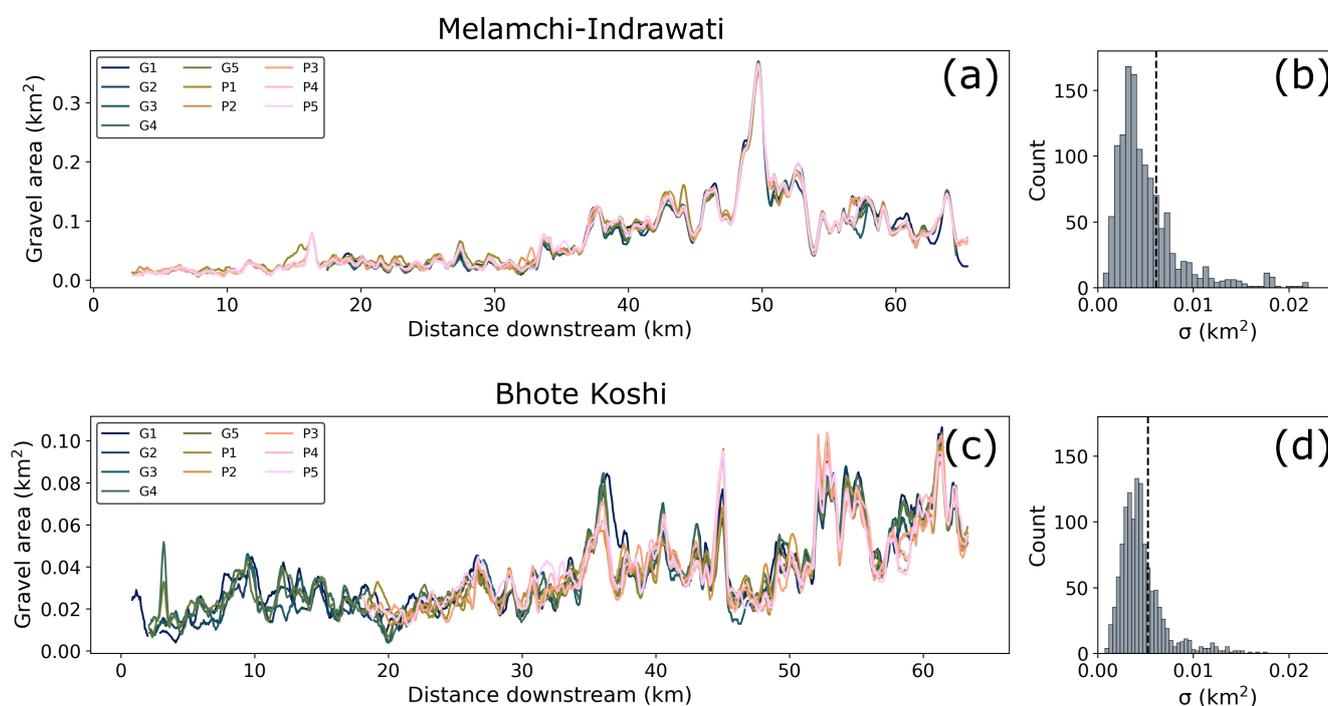
Figure 5. (a) Five versions of both the Google Earth (G1-5) and Planetscope (P1-5) mapped area for Melamchi-Indrawati, 22 April 2018. (b) Histogram of the standard deviations of the ten different measured areas for each data point in A. (c) Five versions of both the Google Earth (G1-5) and Planetscope (P1-5) mapped area for Bhote Koshi, 7/9 December 2017 and 10 December 2017, respectively. Visibility in the Planetscope imagery was too poor to map the section from 0-18 km. (d) Histogram of the standard deviations of the ten different measured areas for each data point in (c), with the 75th percentile indicated by the dashed black line. G = Google Earth; P = Planetscope.

4.2   Coseismic landslide connectivity

Roback et al. (2018) assessed the connectivity of the landslides in their comprehensive inventory and found that just under a third of landslides occurred within 50 m of a fluvial channel, while three-quarters were located within 400 m. Larger landslides, as they tend to have higher runout lengths, are associated with higher connectivity, as are landslides at higher altitude and relief

190 (Roback et al., 2018). While Li et al. (2016) found that 40% by volume of landslides triggered by the 2008 Wenchuan (China) earthquake were connected to river channels, they also noted a strong spatial variation in connectivity, ranging from 20 to 90% between catchments. To test how the connectivity of Gorkha earthquake-triggered landslides in the Melamchi-Indrawati and Bhote Koshi catchments compares to connectivity in Roback et al. (2018)'s study area as a whole, we therefore assess the connectivity of a subset of Roback et al. (2018)'s data set, limited to the Melamchi-Indrawati and Bhote Koshi catchments, and

195 add the inventory of Gnyawali and Adhikari (2017a), which is also available online via the U.S. Geological Survey (Gnyawali and Adhikari, 2017b; Roback et al., 2017). Here, we follow Roback et al. (2018)'s vector-based approach by applying buffer zones around all channels exceeding a threshold drainage area A_c, and tagging all landslide polygons intersecting the buffer as connected to the river network. We set $A_c = 0.48$ km^2, corresponding to the value Roback et al. (2018) found to be the threshold for fluvial channels, and vary the width of the buffer zone from 50 to 400 m. To assess landslide connectivity by

200 volume, we use the area-volume scaling law $V = \alpha A^\gamma$. In their study, Roback et al. (2018) test a wide range of values for the scaling parameters α and γ. We use the median values Roback et al. (2018) report for the scaling parameters based on Himalayan mixed soil and bedrock: $log_{10}(\alpha)$ = -0.59 and γ = 1.36 (Larsen et al., 2010; Roback et al., 2018).

4.3 Valley morphology and channel steepness

We use the topographic analysis package LSDTopoTools (Mudd et al., 2021) to extract river profiles, normalised channel

205 steepness, and valley width along the reaches of the Melamchi-Indrawati and Bhote Koshi considered in this study. The aim of this analysis is to further identify potential zones of sediment storage. For valley width, we use the automated method developed by Clubb et al. (2017) which first identifies floodplains based on channel relief and local gradient before calculating the width of the extracted floodplain at each point in the channel. We apply the floodplain and valley width extraction to a 30 m resolution Copernicus Digital Elevation Model (DEM). In order to limit the likelihood of overestimating channel width,

210 which typically occurs when channels become narrower than a couple of pixels, all tributary channels below a Strahler stream order of 3 are ignored. We calculate normalised channel steepness k_{sn} from the equation $S = k_{sn}A^{-\theta_{ref}}$, where S = channel gradient (dimensionless), A = drainage area (m^2) and θ_{ref} = reference concavity index (dimensionless), and using the statistical approach described in Mudd et al. (2014). The value of θ_{ref} can significantly affect the values of k_{sn} (Gailleton et al., 2021), and we therefore constrain θ_{ref} using the method outlined by Gailleton et al. (2021). This yielded a best fit θ_{ref} value of 0.15

215 for the Melamchi-Indrawati and Bhote Koshi catchments combined. This value is relatively low compared to the global data set shown in Gailleton et al. (2021), which may reflect the importance of debris flows in controlling the long-term shape of the long-profiles in these catchments (e.g. Gasparini et al., 2004; Whipple et al., 2013). Additionally, Gailleton et al. (2021) suggest that the presence of glaciers as well as spatial variations in tectonic processes can obscure the concavity signal.

5   Results

5.1   Determining gravel area along the river channel

The changes in gravel area mapped along the Melamchi-Indrawati rivers as well as the valley width extracted from digital topographic data highlight the transition from a confined river system to a wide and alluvial channel ca. 5 km downstream of Melamchi Bazaar (Fig. 6b, d), with valley width reaching 1000 m at 45 km. No such signal is seen along the Bhote Koshi (Fig. 7b, d), with valley widths not exceeding 200 m for the full length of the studied reach. Gravel area along the Bhote Koshi is lower than along the Melamchi-Indrawati rivers in absolute terms, and does not show significant spatial variations. Gravel area along both mapped rivers shows temporal noise across all mapping epochs; this is most pronounced in the reach extending from 40 to 60 km along the Melamchi-Indrawati rivers (Figs. 6b, c). At 37 km downstream along the Bhote Koshi, an increase in gravel area between February 2013 and May 2015 is visible (Fig. 7b, c). This peak persists over the subsequent mapping epochs, attenuating slightly beginning in October 2020. The timing and location of this signal is consistent with the 2014 Jure landslide (Acharya et al., 2016; Croissant et al., 2017; van der Geest, 2018).

Following the Gorkha earthquake (i.e. from the May 2015 to Jan/Feb 2016 mapping epochs), both rivers experienced localised increases in gravel area. Although the mainshock of the Gorkha earthquake series pre-dates May 2015 imagery, the time interval is short enough that we would not expect the majority of coseismic landslide sediment to have yet been delivered to the river network, or to have been transported a significant distance. The most prominent increase in gravel area following the Gorkha earthquake is seen at Timbu (Figs. 1 and 6a, b, c), where the Melamchi River received an influx of sediment from a debris flow in a tributary channel, as shown in Fig. 3; this peak persists until early 2020. Neither the Melamchi-Indrawati nor the Bhote Koshi show any signals that could be linked in space or time to the hydro-geomorphic events outlined in Section 3.2, such as the 2016 Bhote Koshi GLOF, until the 2021 event. From June to July 2021, there is a marked, consistent increase in gravel area along the Melamchi-Indrawati rivers from just upstream of Timbu to ca. 5 km downstream of Melamchi Bazaar (Fig. 6b, d).

From June to July 2021, the maximum increase in gravel area observed is 0.18 km^2 at ca. 37 km (i.e. downstream of Melamchi Bazaar), which coincides with the furthest downstream extent of the continuous signal and a marked increase in valley width (Fig. 6b, c, d). Although the spatially continuous increase in gravel area stops at the transition to a wider alluvial valley, localised increases of up to 0.08 km^2 are observed along the remaining study reach until Dolalghat. The location and timing of this signal is consistent with field reports documenting the aftermath of the 15 June 2021 Melamchi disaster (Baskota et al., 2021; Pandey et al., 2021) (Section 3.2), which is reaffirmed by this signal being absent in the Bhote Koshi (Fig. 7). Immediately upstream of Melamchgaon, a local increase in gravel area between June and July 2021 of ca. 0.1 km^2 is observed in July 2021, and the resulting peak persists until the last mapping epoch in December 2021. In the same time period, Baskota et al. (2021) and Pandey et al. (2021) document a reactivation of a landslide at Melamchigaon, which briefly dammed the Melamchi River, thereby contributing to the scale of the June 2021 Melamchi disaster. Between July and December 2021, we observe additional increases in gravel area between Timbu and Chanaute Bazaar, and the July 2021 peak translates several kilometres more downstream, to the approximate location of the MCT at 40 km along our study reach (Fig. 6b, c). In summary,

no significant continuous signals in either the spatial or temporal dimension are observed along the Bhote Koshi. The first and only such signal is observed along the Melamchi-Indrawati rivers in July 2021, following the June 2021 Melamchi disaster, and persists until the end of our mapping period. While some changes in gravel area along both rivers could be attributed to the initial impact of additional sediment yield in the six years following the Gorkha earthquake, these are localised and small by comparison with the impact of the 2021 Melamchi event.
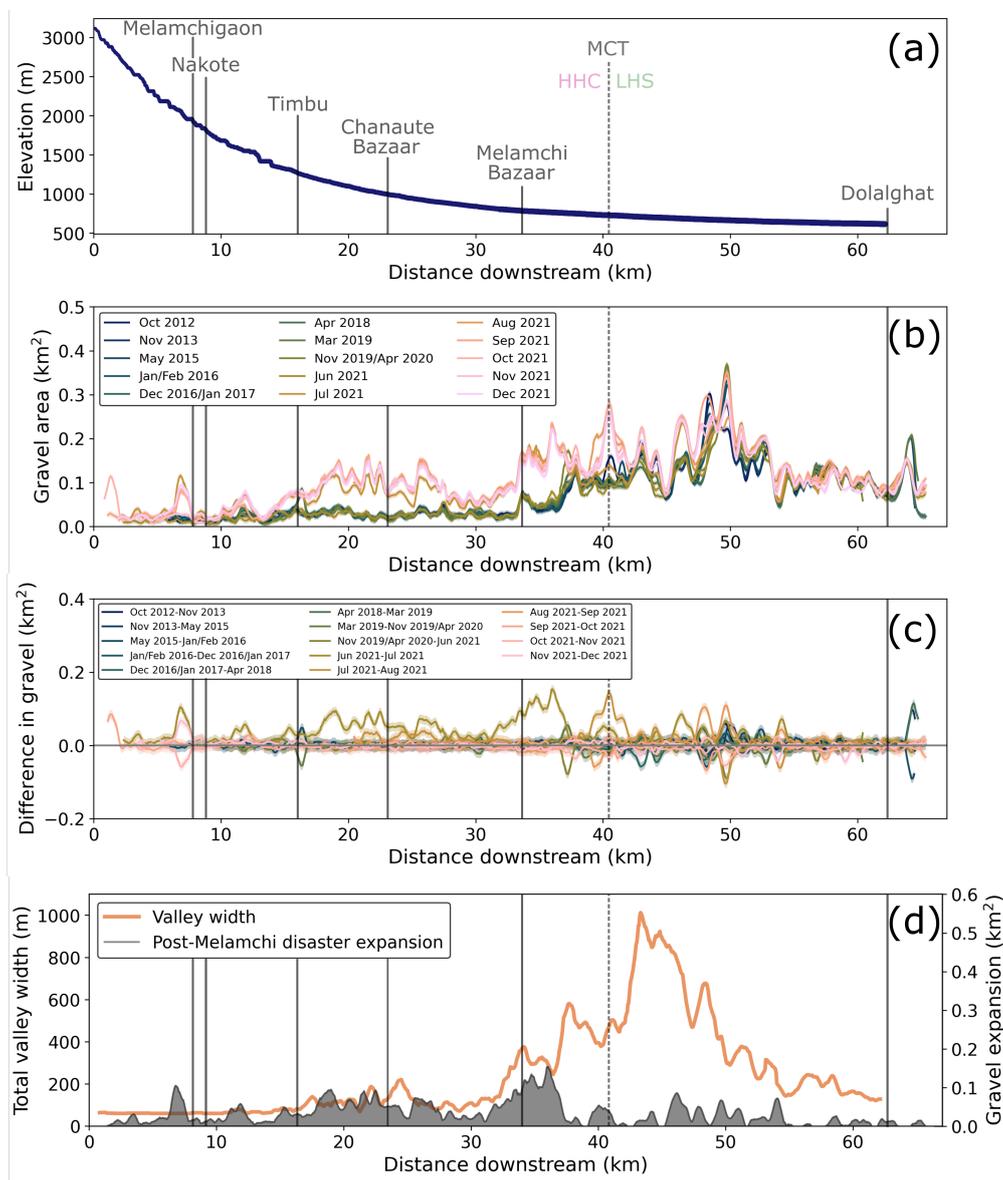
Figure 6. Changes in gravel area along the Melamchi-Indrawati rivers: (a) Long-profile of Melamchi-Indrawati river within the study area; (b) Mapped gravel area along profile; (c) Difference in mapped area along profile between each time period; (d) Valley width extracted with LSDTopoTools plotted alongside mapped expansion in gravel between June and July 2021 (i. e. before and after the Melamchi event). Areas until November 2019/April 2020 inclusive mapped in Google Earth Pro; areas from June 2021 onward mapped in QGIS from Planetscope imagery. Locations mentioned in the text are labelled in (a) and shown with vertical grey lines. Dashed grey line indicates approximate location of Main Central Thrust (MCT), separating the Higher Himalayan Crystallines (HHC) from the Lesser Himalayan Sequence (LHS).
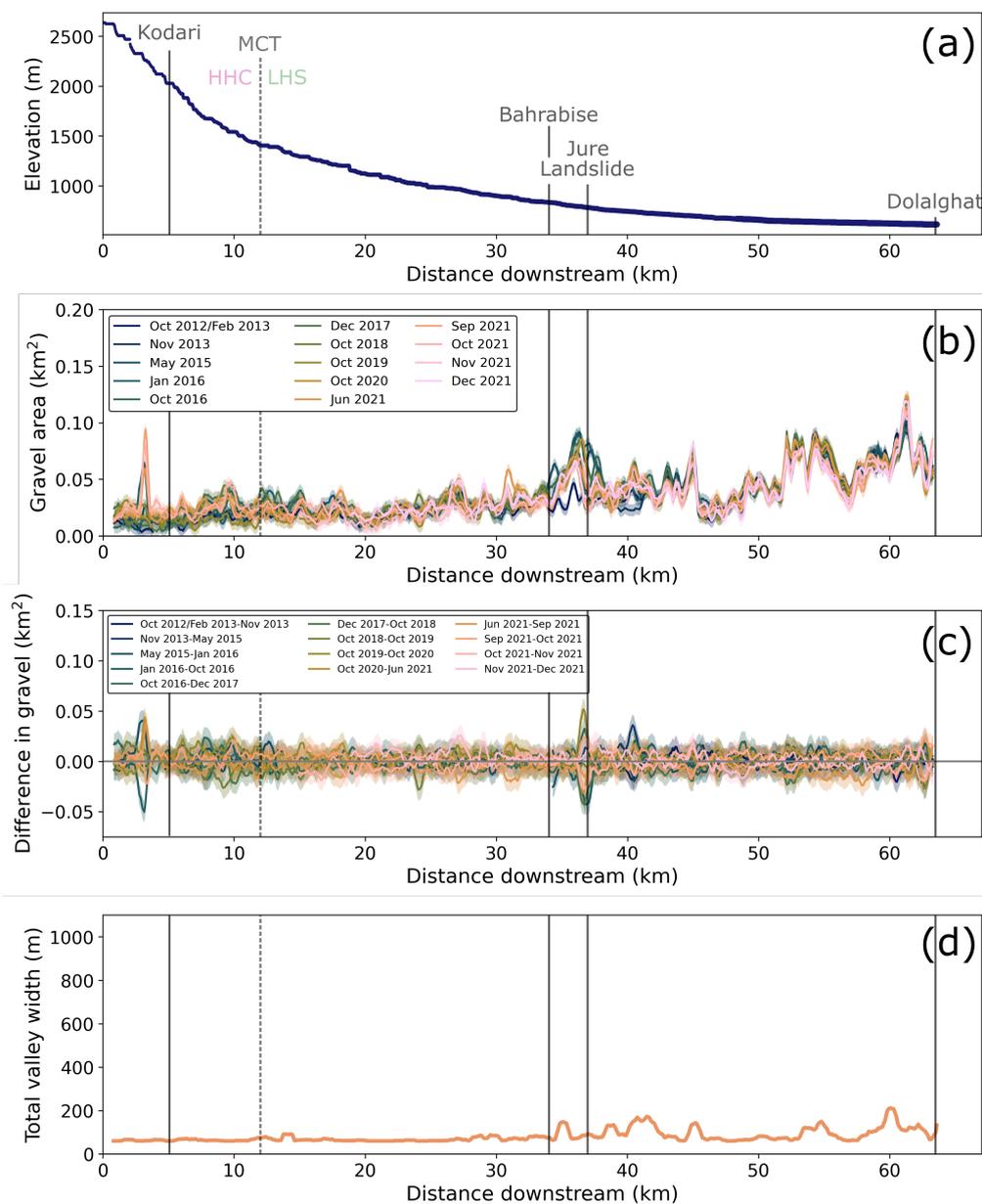
Figure 7. Changes in gravel area along the Bhote Koshi: (a) Long-profile of Bhote Koshi within the study area; (b) Mapped gravel area along profile; (c) Difference in mapped area along profile between each time period; (d) Valley width extracted with LSDTopoTools. Areas from October 2016 and October 2018 onward mapped in QGIS from Planetscope imagery; all other areas mapped in Google Earth Pro. Locations mentioned in the text are labelled in (a) and shown with vertical grey lines. Dashed grey line indicates approximate location of Main Central Thrust (MCT), separating the Higher Himalayan Crystallines (HHC) from the Lesser Himalayan Sequence (LHS).

5.2 Coseismic landslide connectivity

We determined the connectivity of the Gorkha earthquake-triggered landslides mapped by Gnyawali and Adhikari (2017a) and
260 Roback et al. (2018) in the Melamchi-Indrawati and Bhote Koshi catchments by number, volume, and area (Fig. 8).
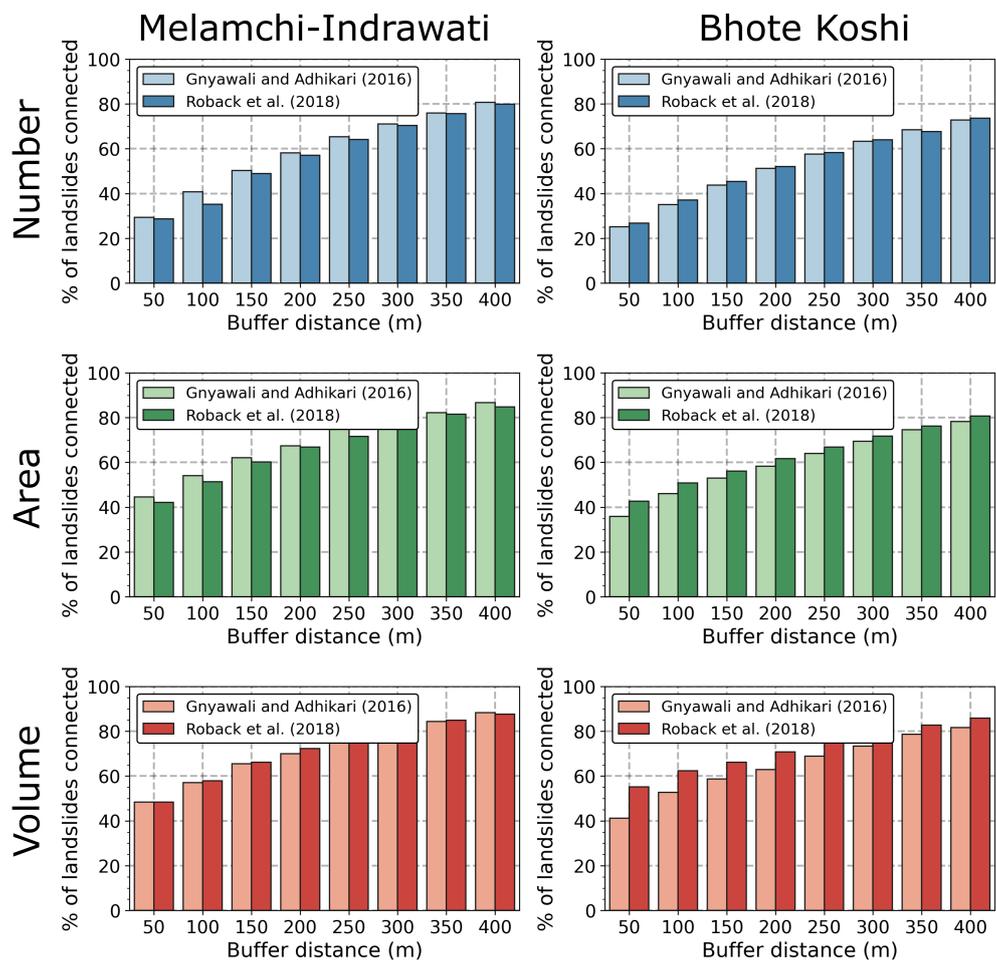
Figure 8. Percentage of landslides triggered by the 2015 Gorkha earthquake connected to the fluvial network, by number (top), area (centre) and volume (bottom) in the Melamchi-Indrawati and Bhote Koshi catchments. The fluvial network is defined here as all channels exceeding a threshold drainage area $A_c = 0.48$ km^2 and a buffer zone of widths ranging from 50-400 m created around the channels. A landslide polygon intersecting a given buffer zone is deemed connected to the river network.

In terms of the connectivity between the rivers and Gorkha induced landslides, our results agree with Roback et al. (2018)'s, suggesting that landslide-channel connectivity is comparable in the Melamchi-Indrawati and Bhote Koshi catchments relative to the full area mapped by Gnyawali and Adhikari (2017a) and Roback et al. (2018). It is worth noting that both landslide inventories assessed here contain only landslides mapped in the immediate aftermath of the Gorkha earthquake (26 April to

265 15 June 2015 in the case of Roback et al. (2018)), and we therefore cannot gain an insight into the temporal evolution of connectivity in our study catchments. Moreover, merely determining whether a landslide is connected to the river network or not is not sufficient for quantifying its impact on the sediment dynamics of the river. For this, it is necessary to determine the extent of the connection (i.e. length of connection), estimate the volume of sediment that can be delivered to the channel, and determine how mobile this sediment is, as regular flows may not be able to mobilise the wide range of grain sizes provided by

270 a landslide or debris flow (Korup 2005).

5.3 Valley width and channel steepness

As shown in Figs. 6d and 7d and further highlighted in Fig. 9a and 9b, the Melamchi-Indrawati and Bhote Koshi rivers show clear differences in valley width along-profile. While the Melamchi-Indrawati transitions from a confined river system to a wide, alluvial channel at ca. 37 km, with valley width reaching 1000 m at 45 km, valley width remains comparatively constant

275 along the studied reach of the Bhote Koshi and does not exceed 200 m. The spatial distribution of normalised channel steepness in the Melamchi-Indrawati catchment follows the expectations established by the pattern of total valley width: the headwaters are steepest, and the wide alluvial section of the Indrawati River downstream of Melamchi Bazaar has the lowest gradient. In the Bhote Koshi catchment, the pattern of normalised channel steepness is slightly more complex. The lowest gradients are present in the headwaters on the Tibetan Plateau as well as the lower reaches near the confluence with the Indrawati River. In

280 the section around the Nepal-China border, the tributary channels and trunk channel show the steepest gradients. The spatial distribution of normalised channel steepness in the Balephi River (adjacent to the Melamchi-Indrawati catchment) mirrors that seen in the Melamchi-Indrawati catchment, with the highest gradients in the headwaters and smaller tributaries and the gentlest channel slopes in the lower reaches. In the headwaters of the Melamchi River, Fig. 9a and 9b show a wide (>300 m) section with low gradient compared to the adjacent reaches. Downstream of this section, the valley narrows to <50 m again,

285 and normalised channel steepness abruptly increases. There is a similar configuration (i.e. a wide, flat section abruptly followed by a narrow and steep channel) in the neighbouring Yangri valley, also indicated in Fig. 9a and 9b. Our preliminary analysis shows no such configurations in the Bhote Koshi catchment or elsewhere in the Melamchi-Indrawati catchment.
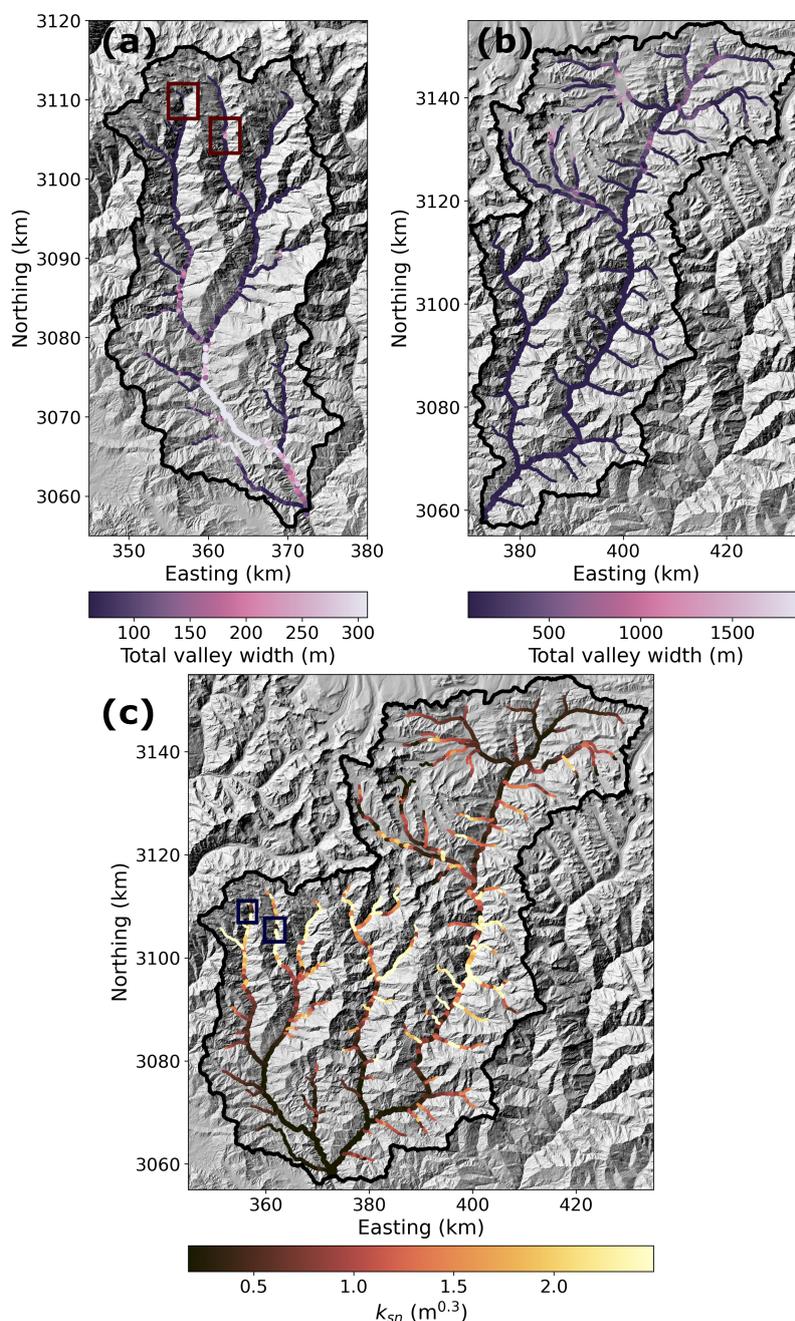
Figure 9. (a) Total valley width in the Melamchi-Indrawati catchment. (b) Total valley width in the Bhote Koshi catchment. (c) Normalised channel steepness k_{sn} in the Melamchi-Indrawati and Bhote Koshi catchments, using a best fit value of $\theta_{ref} = 0.15$ for the combined catchments. Boxes in the headwaters of the Melamchi and Yangri rivers in panels (a) and (c) outline a similar anomalous configuration: a wide, flat reach followed by a narrow and steep reach (see discussion and Fig. 11). To extract the channel network for this figure, we selected a drainage area threshold of 15,000 pixels (or 13.5 km^2, as pixels are 30x30 m). The minimum and maximum values of the colour bars in all panels are set to the 10th and 90th percentile, respectively, of the data shown. Background of all three panels is a shaded relief map derived from a 30 m Copernicus DEM.

6   Exploration of the Melamchi event

Our mapped gravel areas along the Melamchi-Indrawati and Bhote Koshi rivers show temporal noise throughout the mapping
290   period from 2012-2021, indicating that the two river systems are not static and gravel bars shift over time. Although we note
several localised increases in gravel area following the Gorkha earthquake, potentially linked to input of coseismic landslide
sediment, these changes are small compared to the significant increase in gravel area along the central reaches of the Melamchi-
Indrawati rivers in the months following the June 2021 Melamchi disaster, or in the Bhote Koshi following the Jure landslide
(Figs. 6 and 7). In the following analysis, we assess whether the Gorkha earthquake was a necessary pre-condition for the 2021
295   Melamchi disaster. We do this by considering the causes of the Melamchi disaster and the source of its sediment.

6.1   Reporting of Melamchi disaster

At the time of writing, three detailed reports documenting the impact of the Melamchi disaster and exploring its causes have
been published (Baskota et al., 2021; Maharjan et al., 2021; Pandey et al., 2021). We summarise these reports, and support
them with photographs taken during a subsequent helicopter flight to the region in December 2021. The initial report from
300   Pandey et al. (2021) describes the event as an outburst flood from a landslide dam triggered by intense localised rainfall.
The Department of Hydrology and Meteorology's (DHM) Sermathang station, 5 km ESE of Timbu, did record higher than
normal cumulative rainfall in the six days preceding the event (Maharjan et al., 2021) and Global Precipitation Measurement
(GPM) data shows high precipitation around Melamchi Bazaar on 14 June (Pandey et al., 2021); however, neither of these
measurements are considered extreme enough to explain the scale of the event.
305   Maharjan et al. (2021) and Baskota et al. (2021), with the benefit of additional information from satellite imagery and
further field excursions, rule out a single trigger, instead listing multiple factors as a cause of the event. They propose a chain
of events culminating in the Melamchi disaster: first, collapse of glacial moraine in the Pemdang Khola which is a tributary
of the Melamchi River; heavy rainfall or high snowmelt released a wave of glacial lake water and glacial sediments. The
resulting debris accumulated in Bremthang, a wide sandy plain downstream of the confluence between the Pemdang Khola and
310   Melamchi Khola (Baskota et al., 2021; Maharjan et al., 2021), which itself has been interpreted as a valley fill behind an old
landslide dam (Maharjan et al., 2021). The floodwaters and debris released in the Pemdang Khola incised into the Bremthang
old dam, mobilizing additional sediment and causing a debris flow that contributed to bank erosion and hillslope toe cutting
further downstream. At Melamchigaon, an old landslide which was reactivated first by the Gorkha earthquake, and subsequently
during this event, is also thought to have dammed the river; the nearby gauging station at Nakote recorded a decrease in water
315   level followed by a rapid increase before the station was destroyed during the event and stopped recording (Baskota et al.,
2021; Pandey et al., 2021). Baskota et al. (2021) point out that the Melamchigoan landslide dam could have retained 32,400-
43,200 m^3 of water, taking into account the decrease in water level recorded at Nakote station and assuming a discharge of
9-12 m^{3}s^{-1}. This amount is small compared to the 70 million m^3 of debris deposited around Melamchi, highlighting that while
the Melamchigaon landslide dam outburst likely added to the disastrous scale of the event, it cannot be the sole cause of the
320   disaster.

While Maharjan et al. (2021) cannot link the Melamchi event to the 2015 Gorkha earthquake with certainty, they suggest that the earthquake destabilised the hillslopes in the area affected by coseismic landsliding during the earthquake, as corroborated by Kincey et al. (2021), who show increased landslide activity since the earthquake.

To summarise, the previous studies have demonstrated the compound nature of the Melamchi disaster, but as yet, have
325   not tackled the question of whether these processes were conditional on sediment released from hillslopes by the Gorkha earthquake.

6.2   Sediment source derived from satellite data

Planet Explorer 3.7 m optical satellite imagery was used to explore the likely sources of sediment during the Melamchi disaster. The satellite data confirm the break-out of the Pemdang Lake, and the accumulation of fresh sediment observed in the Bhe-
330   mathan valley. But the data also show widespread sediment excavation in a number of neighbouring valleys in the catchment, suggesting increased discharge over a broad area rather than a point source (Fig. 10). For example, many of the channels in the upper Yangri Valley, immediately east of Melamchi, also show evidence of expansion of sediment accumulation, as does a smaller valley to the west. The location at which the headwaters of these channels were reactivated falls between an eleva-tion range of approximately 4500-4800 m elevation, and extends along the range for at least 10 km between the valleys in an
335   WSW-ENE orientation. Critically, the source locations for the initiation of sediment mobility are not locations characterised by intense landsliding in response to the Gorkha earthquake.

These observations support the interpretations from previous reports that suggest a single dam failure or outburst event is insufficient to explain the volumes of discharge and sediment recorded in the Melamchi valley. Instead, the evidence of sediment mobilisation in multiple catchments along the range implies an intense precipitation event that was too localised to be
340   picked up by any of the meteorological stations. Overtopping and release of the Pandam Lake accompanied by rapid incision of the old landslide that dammed the Bhemathan Valley were a part of the response to this rainfall event that added to its impact. A similar 'cloudburst' event caused devastation in the Ladakh Himalaya in 2010 where both the meteorological stations and radar satellite data missed the rainfall as it was localised over a 6 km wide zone that run between multiple small catchments along strike at an elevation of approximately 4500 m (Hobley et al., 2012). An additional conclusion is therefore that the Melamchi
345   disaster appears to have been independent of the Gorkha earthquake, as there is no evidence that the main sources of sediment have been pre-conditioned by the Gorkha earthquake, although the river damming and dam outburst at Melamchigaon likely amplified the impact of the flood.
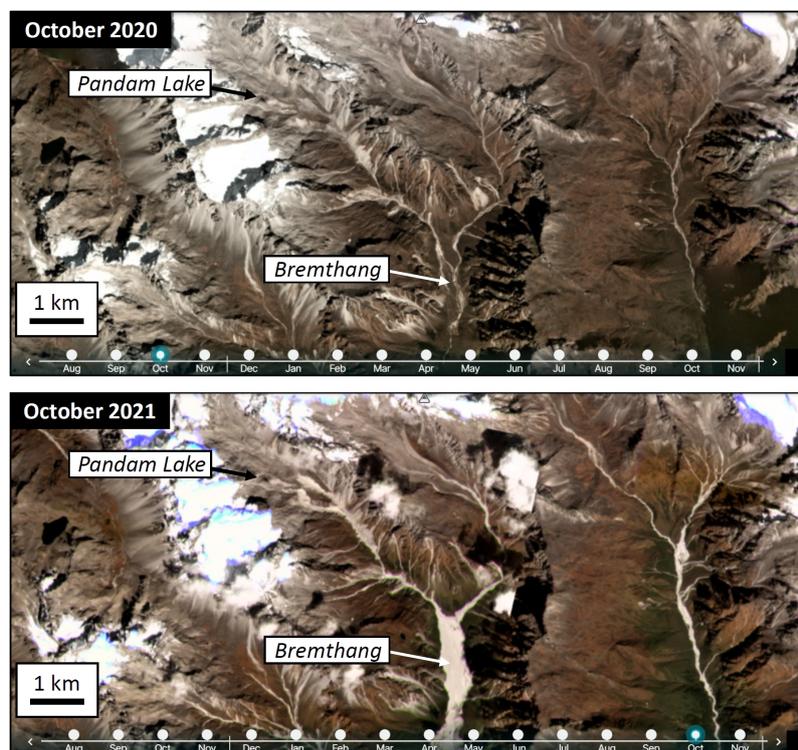
Figure 10. Planet Explorer imagery of the headwaters of the Melamchi-Indrawati catchment (Planet Team, 2017), used to identify potential sources of sediment during the 2021 Melamchi flood event. Comparison between clear day images before and after the event are used to identify zones of sediment mobilization. Throughout the monsoon period from mid-June to mid-September, most of the region is cloud-covered. We therefore chose to compare the images from October 2020 to those of October 2021, encompassing the full monsoon season of 2021, including the Melamchi disaster. Valleys characterised by excavation of sediment by active channels are highlighted by bright white or grey tones.

7 Discussion

7.1 Landslide connectivity following the 2015 Gorkha earthquake

350 It is possible that large-scale channel aggradation such as that observed following the 1999 Chi-Chi (Taiwan) and 2008 Wenchuan (China) earthquakes (Chen and Petley, 2005; Whadcoat, 2011; Yanites et al., 2010) did not happen in the aftermath of the Gorkha earthquake because the landslides were not connected to active river channels to the same extent (Collins and Jibson, 2015; Cook et al., 2016). A landslide connected to the river network will deliver sediment to the channel and therefore contribute to an increase in sediment load downstream, whereas a landslide isolated on a hillslope and not connected

355 to the fluvial domain will not immediately contribute to the fluvial sediment budget. Fig. 8 shows that the connectivity in both studied catchments is consistent with that found by Roback et al. (2018)'s across a broad area affected by the Gorkha

earthquake, and it is therefore unlikely that low connectivity is the reason for the lack of coseismic landslide sediment in the
river channels. However, whether a landslide ends up contributing to the sediment budget will also depend on how quickly it
becomes re-stabilized, mostly through re-vegetation, although the landslide mass will likely remain more easily re-mobilised
360 than an intact hillslope. Re-vegetation of hillslopes can occur rapidly in tropical and/or wet climates. For example, Lin et al.
(2007) reported 66% of vegetation recovering in four years following the 1999 Chi-Chi earthquake, and Saba et al. (2010)
demonstrated that hillslopes had re-vegetated and stabilised within two years of the 2005 Kashmir earthquake – much earlier
than expected – facilitating a rapid return of landslide activity to pre-earthquake conditions. Fan et al. (2018) and Gan et al.
(2019) showed that hillslopes returned to pre-earthquake conditions between seven and nine years after the 2008 Wenchuan
365 earthquake, with Fan et al. (2018) citing re-vegetation, grain coarsening and densification of the mass wasting deposits as the
main processes promoting rapid hillslope stabilisation. Based on these observations, Fan et al. (2018) suggest that long-term
hillslope processes contribute significantly more to mass removal following large earthquakes than short-term mass wasting
processes.

In the area affected by coseismic landsliding during the 2015 Gorkha earthquake, Kincey et al. (2021) compiled a multi-
370 temporal landslide inventory over eleven mapping epochs, from pre-monsoon 2014 to post-monsoon 2018. For each 1 km^2
grid cell in their mapping area, landslide "birth" was assigned to the first epoch in which the cell was first impacted by a
landslide, and landslide "death" indicated the epoch in which the cell was last impacted by a landslide. Although Kincey
et al. (2021) did not assess hillslope stability or re-vegetation patterns, they showed that in ca. 75% of the cells registering a
coseismic landslide birth, the landslides persist until the final mapping epoch, after the 2018 monsoon. This tentatively suggests
375 that hillslopes had not yet extensively re-vegetated in the three years following the 2015 Gorkha earthquake. These findings
therefore suggest that the lack of large-scale aggradation following the Gorkha earthquake cannot be attributed to anomalously
low connectivity or rapid re-vegetation in the studied area. In the following sections, we discuss the importance of alternative
controls on downstream sediment transfer, including major hydrological events and valley morphology.

7.2 Importance of hydro-meteorological events for sediment export

380 Following the 1999 Chi-Chi earthquake in Taiwan, Typhoon Toraji (2001) resulted in a three-fold increase in landslide area
compared to pre-earthquake Typhoon Herb even though the latter brought more rainfall (Lin et al., 2004, 2006). Previous studies
following large earthquakes note elevated suspended sediment loads for several years following the event itself, suggesting that
further triggering events beyond the earthquake itself are needed to flush out coseismic landslide sediment (Dadson et al., 2004;
Yanites et al., 2010; Hovius et al., 2011). In their study focusing on the Wenchuan earthquake, Wang et al. (2015) additionally
385 found that the residence time of coseismic landslide sediment in catchments is reduced by periods of intense rainfall such as
tropical cyclones.

The volume of coseismic Gorkha landslides connected to a fluvial channel in the Melamchi-Indrawati valley, calculated in
Section 4.2, ranges from 26 to 48 million m^3 and from 43 to 77 million m^3 based on the landslide inventories of Gnyawali and
Adhikari (2017a) and Roback et al. (2018), respectively, with the lower end of the range indicating landslides within 50 m of a
390 channel and the upper end including all landslides within 400 m of a channel. Based on these calculations alone, it is therefore

possible that Gorkha landslides contributed a significant amount of the 13 million m^3 deposited between Nakote and Dolalghat (Maharjan et al., 2021) during the 2021 Melamchi flood. However, these are likely overestimates since our calculations account for all landslides connected to channels with a drainage area exceeding 0.48 km^2 in the whole Melamchi-Indrawati catchment, and therefore are not limited to only those landslides that would have been able to supply sediment directly to the reach of the Melamchi River affected by the June 2021 event. In addition, it is unlikely all sediment produced through landsliding would become mobilised during one flood event.

The triggers of the Melamchi event proposed by Baskota et al. (2021) and Maharjan et al. (2021), indicate that the majority of the sediment involved in the June 2021 event was sourced from an area in the catchment than was located higher than the area that had been worst affected by Gorkha earthquake-triggered landslides, suggesting that hillslope pre-conditioning by the earthquake likely played only a minor role in facilitating the Melamchi disaster. Analysis of the Planet Explorer images confirms this origin and highlight that sediment mobilisation likely occurred as a result of an extreme hydro-meteorological event focused on an area across the 4500-4800 m elevation range. The associated glacial lake outburst in the Pemdang Khola, valley damming by the Melamchigaon landslide, and subsequent dam outburst, likely contributed to the severity of the event.

7.3 Importance of valley morphology for sediment export

Our study focused on the Melamchi-Indrawati and Bhote Koshi catchments in central Nepal, both of which experienced severe coseismic landsliding during the 2015 Gorkha earthquake sequence. Additionally, the studied reaches in both catchments flow predominantly across the rocks of the Higher Himalayan Crystallines (HHC) and Lesser Himalayan Sequence (LHS), and are crossed by the Main Central Thrust (MCT). However, the evolution of gravel area during our study period from 2012-2021 is dramatically different between the two catchments, with the Melamchi-Indrawati river experiencing a dramatic increase in gravel area associated with a catastrophic high concentration flow event in June 2021, which persists until the end of our mapping period. In this section, we explore the potential influence of valley morphology and geomorphic history on the occurrence of this event in the Melamchi-Indrawati but not the Bhote Koshi catchment. Baskota et al. (2021), Maharjan et al. (2021), and Pandey et al. (2021) all agree that Bremthang, a wide, sandy plain in the headwaters of the Melamchi River, was a key component of the Melamchi disaster. As Baskota et al. (2021) point out, the low gradient of Bremthang allowed water and debris to accumulate. We therefore hypothesise that the configuration of the Bremthang facilitated the Melamchi disaster, with a flat and wide reach upstream acting as a sediment trap connected to a steep, confined channel allowing rapid evacuation of sediment once the old landslide dam was breached, adding to the catastrophic impact of the event further downstream. As shown in Fig. 9 and 11, the Bremthang is visible in maps of channel steepness and channel width as a wide and flat section abruptly followed by a transition to a steep and narrow channel downstream. We also note that the headwaters of the Yangri River, immediately to the east of the Melamchi River, show a similar configuration, albeit less pronounced than the Bremthang along the Melamchi River (Fig. 11). Landslide dams such as the Bremthang are made of heterogeneous material with wide range of grain sizes, up to very large boulders. They can therefore persist for decades to centuries. By contrast, valley fill accumulating behind a landslide dam is composed of finer grained alluvium and lake sediment (Weidinger, 2006), meaning it can be mobilised relatively easily once the landslide dam is incised. As reported by Baskota et al. (2021), the Melamchi River

425   is currently incising into the downstream end of the Bremthang valley fill, forming a steep scarp whose collapse led to a second debris flow event on 31 July 2021 (Fig. 11d). This further highlights the potential of landslide-dammed valley fill as sediment stores that can be released during extreme hydrological events, and ties in well with Devrani et al. (2015)'s observation from the upper Ganga basin that during extreme events, low-gradient reaches aggrade and high-gradient reaches incise. Our insights from assessing the patterns of valley width and normalised channel steepness in the Melamchi-Indrawati and Bhote Koshi

430   catchments indicate that topographic analysis can help identify sediment stores that may pose a similar risk to the valley fill in the Bremthang, which significantly contributed to the scale of the 2021 Melamchi disaster.
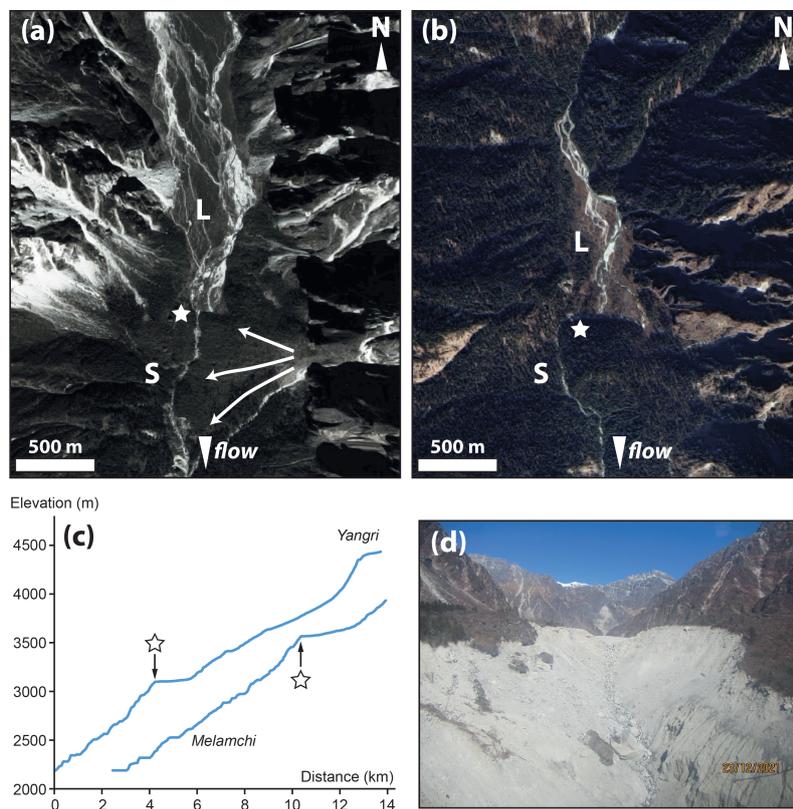
Figure 11. Morphological anomalies and potential sediment stores in the headwaters of the Melamchi and Yangri rivers. (a-b) © Google Map images of areas characterized by wide, low gradient valleys with braided channels (L) abruptly transitioning downstream into steep narrow channels (S) (see boxes in Fig. 9) (©2021 Maxar Technologies). The stars indicate the transition. (a) Bremthang in the Melamchi Valley, interpreted to be a valley fill behind a landslide dam (represented by fanning arrows); the breach of the landslide dam and re-incision of the valley fill is believed to have contributed a significant amount of sediment during the Melamchi disaster. (b) A similar configuration in the Yangri valley immediately east of the Melamchi valley. (c) River profiles showing the location and extent of the low-gradient reaches shown in (a) and (b), and the abrupt transition to a steep reach downstream (indicated by the stars). (d) Photo looking north (upstream) taken from the approximate original location of the knickpoint at the Bremthang (star in (a)), showing rapid incision into valley fill and remobilization of large amounts of sediment during the Melamchi disaster. Approximate location of star in (a) is 28.0930, 85.5461. Approximate location of star in (b) is 28.0658, 85.5963.

8 Conclusions

By producing sediment through widespread mass wasting, large earthquakes are expected to influence fluvial and sediment dynamics for years to centuries. In this study, we have mapped gravel area in the Melamchi-Indrawati and Bhote Koshi catchments in central Nepal from 2012 to late 2021 to assess the impact of the 2015 Gorkha earthquake, which triggered over 25,000 landslides and was expected to result in channel aggradation, in a similar manner as following the 2008 Wenchuan

(China) earthquake which had a similar moment magnitude. However, our data show only localised and small increases in gravel area that can be directly linked to landslides triggered by the Gorkha earthquake. The only clear, reach-scale signal in either catchment is a sharp increase in gravel area from June to July 2021 along a 30 km stretch of the Melamchi-Indrawati

440   rivers, caused by an extreme high concentration flow event on 15 June 2021. We explore the reasons for the absence of a clear signal attributable to the Gorkha earthquake, and assess the influence of the Gorkha earthquake on the 2021 Melamchi disaster, and the potential control of valley morphology on the occurrence of similar events. From a review of field reports following the Melamchi disaster, combined with new analysis of optical satellite data, we find that the majority of sediment transported during the event was sourced from a rainfall event localised in elevation but stretching between neighbouring catchments; the

445   sediment supplied by this event was further upstream than the coseismic landslides. This indicates that a hydro-meteorological trigger played the dominant role in the Melamchi disaster rather than hillslope pre-conditioning by the 2015 Gorkha earthquake. We suggest that extreme climatic events and the existence of sediment stores within valleys, rather than the instability of hillslopes, limit the export of sediment from this part of the Himalaya. We provide guidance to identify such sediment stores which, we believe, pose greater risk to populations than co-seismic landslides in a region increasingly exposed to extreme

450   hydro-meteorological events.

Code and data availability. The mapped shapefiles as well as the code used to process the mapping data are available upon request to the corresponding author. The code and documentation for the valley width extraction code is available at: https://github.com/LSDtopotools/LSDTopoTools2.

Appendix A: Mapping

A1   Imagery dates and sources

Table A1. Imagery dates and sources for Melamchi-Indrawati rivers. Extent refers to distance along the polyline representing the channel and is consistent with the distances shown in Fig. 6. Asterisk indicates imagery used to constrain mapping uncertainty.

Mapping epoch	Date (dd/mm/yy)	Imagery source	Extent
Post-2012 monsoon	28/10/12	Maxar Technologies	5 - 53.5 km
	31/10/12	Maxar Technologies	53.5 - 64.4 km
Post-2013 monsoon	10/11/13	CNES/Airbus	47.2 - 64.4 km
Post-2014 monsoon	03/05/15	CNES/Airbus	5 - 64.6 km
Post-2015 monsoon	30/01/16	Maxar Technologies	53.7 - 64.4 km
	01/02/16	Maxar Technologies	4.9 - 53.7 km
Post-2016 monsoon	28/12/16	CNES/Airbus	51 - 64.4 km
	17/01/17	CNES/Airbus	31 - 51 km
	29/01/17	CNES/Airbus	9 - 31 km
Post-2017 monsoon*	22/04/18	Maxar Technologies	17.2 - 64.4 km
	22/04/18	Planetscope	2.5 - 65.8 km
Post-2018 monsoon	06/03/19	Maxar Technologies	7.1 - 64.4 km
Post-2019 monsoon	28/11/19	CNES/Airbus	9.5 - 28.6 km
	03/04/20	Maxar Technologies	28.6 - 31.7 km
	19/04/20	Maxar Technologies	31.7 - 60.4 km
Post-2020 monsoon	02/06/21	Planetscope	1.6 - 65.8 km
	29/07/21	Planetscope	1.6 - 65.8 km
	11/08/21	Planetscope	20 - 65.8 km
	12/09/21	Planetscope	0.7 - 65.8 km
Post-2021 monsoon	13/10/21	Planetscope	0 - 65.8 km
	14/11/21	Planetscope	2.7 - 65.8 km
	13/12/21	Planetscope	1.6 - 65.8 km

Table A2. Imagery dates and sources for the Bhote Koshi. Extent refers to distance along the polyline representing the channel and is consistent with the distances shown in Fig. 7. Asterisk indicates imagery used to constrain mapping uncertainty.

Mapping epoch	Date (dd/mm/yy)	Imagery source	Extent
Post-2012 monsoon	31/10/12	Maxar Technologies	47.5 - 63.7 km
	13/02/13	Maxar Technologies	0 - 47.5 km
Post-2013 monsoon	10/11/13	CNES/Airbus	41.1 - 63.7 km
Post-2014 monsoon	04/12/15	CNES/Airbus	32.1 - 35.1 km
	03/05/15	CNES/Airbus	35.1 - 63.7 km
	04/05/15	CNES/Airbus	0 - 32.1 km
Post-2015 monsoon	11/01/16	Maxar Technologies	0 - 13.3 km
			19.9 - 30.5 km
			33.9 - 58.3 km
	30/01/16	Maxar Technologies	58.3 - 63.7 km
Post-2016 monsoon	29/10/16	Planetscope	0 - 63.7 km
Post-2017 monsoon*	07/12/17	CNES/Airbus	32 - 33.4 km
	09/12/17	CNES/Airbus	2.2 - 32 km
			33.4 - 63.7 km
	10/12/17	Planetscope	18 - 63.7 km
Post-2018 monsoon	29/10/18	Planetscope	0 - 63.7 km
Post-2019 monsoon	17/10/19	Planetscope	0 - 63.7 km
Post-2020 monsoon	20/10/21	Planetscope	0 - 63.7 km
	02/06/21	Planetscope	0 - 63.7 km
	12/09/21	Planetscope	0 - 63.7 km
Post-2021 monsoon	13/10/21	Planetscope	0 - 63.7 km
	14/11/21	Planetscope	14.4 - 63.7 km
	13/12/21	Planetscope	18.5 - 63.7 km

455 A2 Parameter selection and sensitivity analysis

We tested the influence of each of the five parameters involved in processing the mapping data on the resulting area values. The five parameters and their selected ranges are: (i) the resolution of the raster res_r, varying from 10-70 m at an interval of 10 m, (ii), the distance between the points along the channel line d_s, varying from 10 - 100 m at an interval of 10 m, (iii) the window distance along the channel d_p, varying from 200 to 1100 m at an interval of 100 m, (iv) the window distance orthogonal to the 460 channel d_o, varying from 200 to 2000 m at an interval of 200 m, and (v) the size k of the rolling window to smooth the area for plotting, for which we used values of 2, 5, 7, and then ranging from 10 - 70 at an interval of 10.

We varied each parameter in turn by the ranges given above, while keeping all other parameters constant. We then processed all areas mapped from Planetscope imagery along the Melamchi-Indrawati rivers and, for each data point along the river, we plotted the corresponding area calculated for the lowest chosen parameter value against that calculated using the highest parameter value (Fig. A1). Assuming that a given parameter does not influence the results, the data plotted should lie along the 1:1 line. Additionally, we show the variation in gravel area along the Melamchi-Indrawati river in one mapping epoch, October 2020, for the full range of each parameter (Fig. A2).

Raster resolution res_r has no discernible influence on the results, with the data points in Fig. A1 lying along the 1:1 line, and we therefore chose 40 m as the final value as this allows for low computational cost while also faithfully reproducing the shape of the mapped areas. The step distance for resampling the channel line to points, d_s follows a roughly linear trend, albeit with some scatter. It is interesting that, as opposed to raster resolution, the epochs do not all follow the same trend. However, Fig. A2b shows that changes in the gravel area along the river channel as a function of d_s are negligible and we could freely choose the value to be used in the processing. We decided on 50 m as it breaks the channel into enough points to accurately sample the river course while also not taking up too much computing time. Window distance along the river, d_p, is not expected to follow a 1:1 trend since the longer the window, the longer the stretch of river that is being sampled in any given window, and therefore the larger the area within this window. However, the data points here closely follow a linear trend which remains consistent across mapping epochs, and Fig. A2c shows that the overall trend does not change. Window distance orthogonal to the river, d_o, is a special case as evidenced by the cut-off seen on the plot, indicating that for $d_o = 200$, the area calculated within each window never exceeds 0.15 km². This is because the widest parts of the mapped channel will exceed 200 m in width and the window will therefore not be able to capture the full extent of the combined channel area (Fig. A2d). To choose the best value for d_o, we therefore needed to make sure that it is at least the width of the widest part of the channel in any time period in order to not lose information. However, setting d_o too high causes more overlap between sections of the river that are not adjacent, e.g. at bends in the river course, and would therefore likely overestimate the area within a given window. Fig. A3 shows the change in total calculated area along the river as a function of d_o. The "roll-off" apparent in this figure indicates the value of d_o beyond which no information is lost due to missing the edges of the active channel, which correlates with the manually derived value of the widest channel section, 800 m. In order to have an extra safety margin, we chose a value of $d_o = 1000$ m. The size of the rolling window for smoothing the data, k, also shows a complex impact on the results, as evidenced by the different trends in each mapping epoch (Fig. A1e). For this case, we again refer to Fig. A2e, which shows that while high values of k remove local signals and translate peaks in gravel area downstream, this does not happen for $k<=10$. The final value chosen ($k = 7$) was based on visual estimation of the smallest value which would sufficiently reduce noise in the data while not removing local signals.

A3 Handling incomplete imagery

For some dates, imagery either did not cover the entire study area or visibility was not good enough to reliably map the rivers (see Tables A1 and A2). The latter was particularly a problem for Planetscope images in the upper reaches of the study area, and especially in the Bhote Koshi, since the NE-SW orientation and steep flanks of the valley create shadows. Where imagery
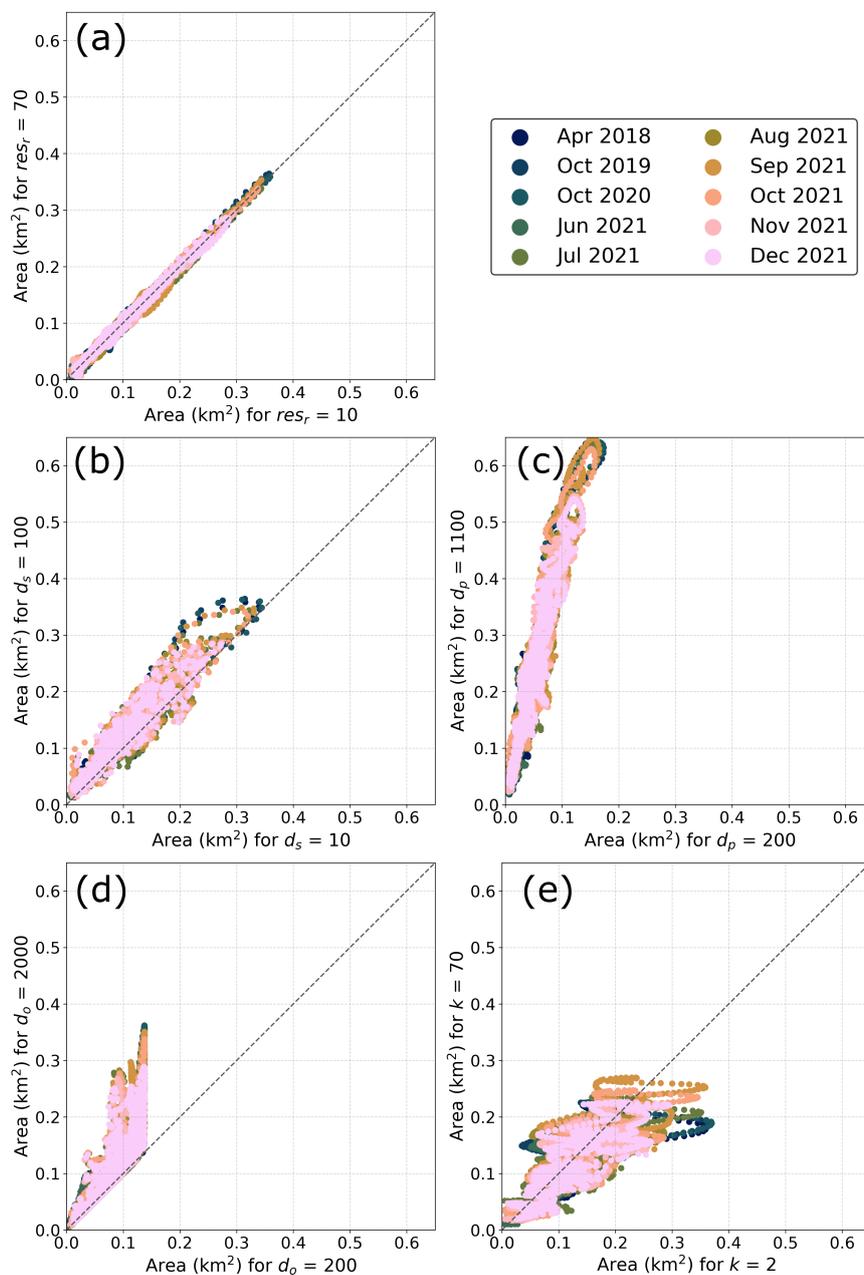
Figure A1. For each of the five parameters we varied in the sensitivity analysis, the area calculated at each channel point using the highest value in the parameter range is plotted against the area calculated using the lowest value in the parameter range. The choice of parameter value is considered to not influence the results if the data points lie along the grey dashed 1:1 line diagonally crossing the plot, as is the case with raster resolution in panel (a). Areas in these plots are mapped from Planetscope imagery along the Melamchi-Indrawati rivers. See the text for a detailed discussion of the results shown here, including the special cases of d_o and d_p.
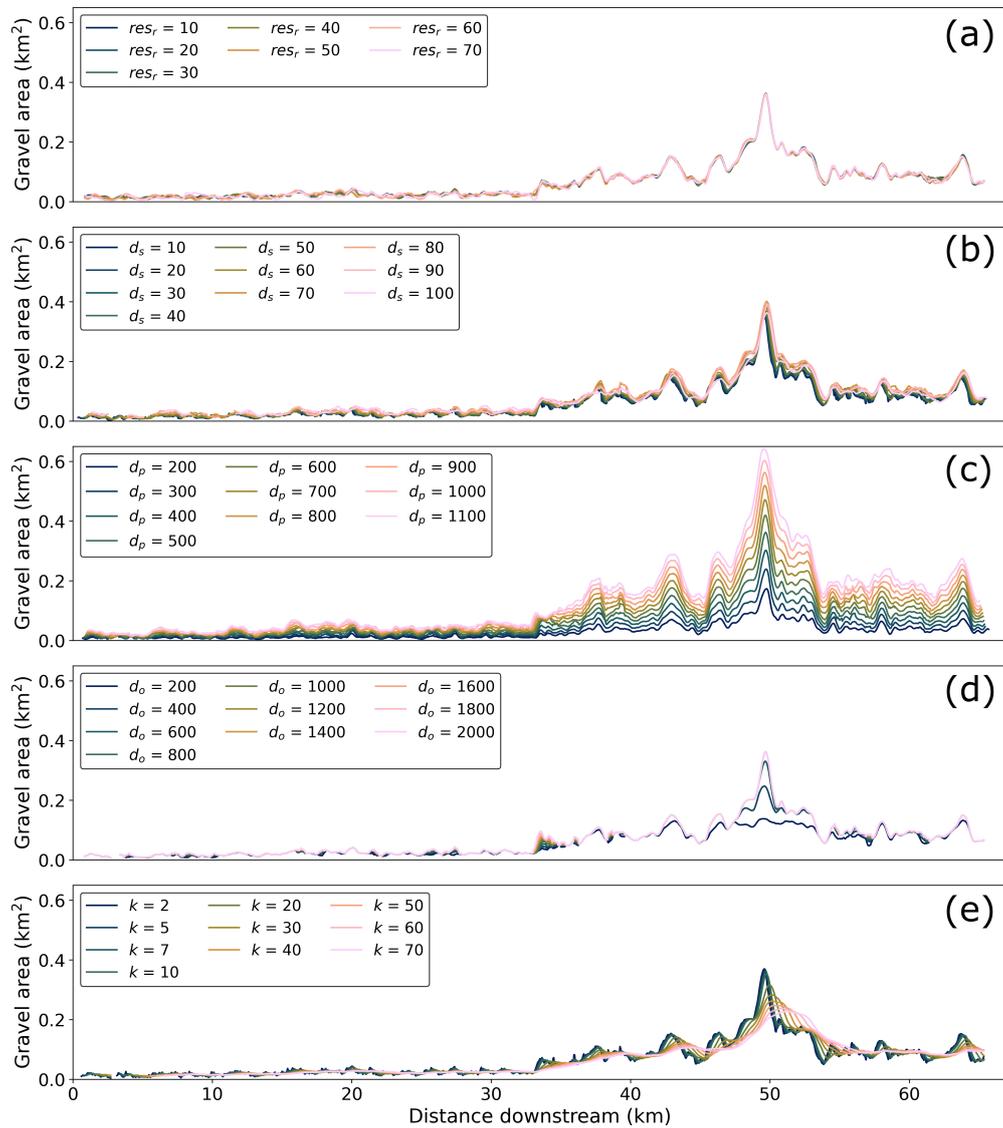
Figure A2. Area along profile for one mapping epoch, showing variation between parameter values. Areas are mapped along the Melamchi-Indrawati rivers from Planetscope imagery of 30/10/2020.
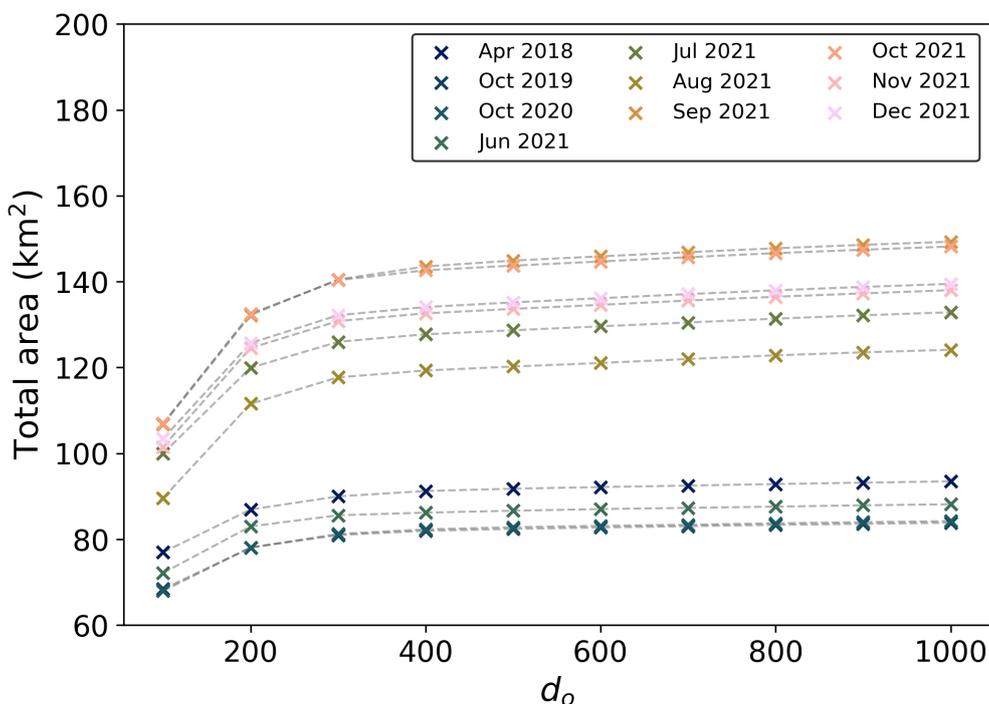
Figure A3. Total gravel area calculated along the Melamchi-Indrawati river as a function of d_o. The roll-off on the graph helps to identify the value of d_o above which we include the full width of the gravel areas. The more that value is exceeded, the more likely it is to get overlap between windows at bends in the river. Areas in these plots are mapped from Planetscope imagery of 30/10/2020 along the Melamchi-Indrawati rivers

was not available or not sufficiently clear, these areas were not included in the data set. Since the figures in the results section show averaged mapped areas along the profile, it was necessary to ensure that the shorter sections of mapped area did not produce erroneous spikes. To that end, we removed the mapped area within one d_p (i.e. 500 m) of either end of the mapped reach prior to smoothing the data with a rolling window.

500   *Author contributions.* HDS, MA, and ELSG conceptualised the study. BG wrote the code to calculate gravel area along channels. ELSG carried out the mapping and valley width extraction and wrote the paper with contributions from all authors.

Competing interests. The authors declare that they have no conflict of interest.

Acknowledgements. ELSG was supported by NERC grant NE/L002558/1. The authors thank Simon Mudd and Jack Blunt for helpful discussions. The scientific colour maps acton, batlow, batlowW and lajolla (Crameri, 2018) are used in this study to prevent visual distortion

505   of the data and exclusion of readers with colour vision deficiencies (Crameri et al., 2020).

References

Acharya, T. D., Mainali, S. C., Yang, I. T., and Lee, D. H.: Analysis of Jure landslide dam, Sindhupalchowk using GIS and Remote Sensing, International Archives of the Photogrammetry, Remote Sensing and Spatial Information Sciences - ISPRS Archives, 41, 201–203, https://doi.org/10.5194/isprsarchives-XLI-B6-201-2016, 2016.

510 Ao, M., Zhang, L., Dong, Y., Su, L., Shi, X., Balz, T., and Liao, M.: Characterizing the evolution life cycle of the Sunkoshi landslide in Nepal with multi-source SAR data, Scientific Reports, 10, 1–12, https://doi.org/10.1038/s41598-020-75002-y, 2020.

Avouac, J. P.: Dynamic Processes in Extensional and Compressional Settings - Mountain Building: From Earthquakes to Geological Deformation, Treatise on Geophysics, 6, 377–439, https://doi.org/10.1016/B978-044452748-6.00112-7, 2007.

Avouac, J. P., Meng, L., Wei, S., Wang, T., and Ampuero, J. P.: Lower edge of locked Main Himalayan Thrust unzipped by the 2015 Gorkha
515 earthquake, Nature Geoscience, 8, 708–711, https://doi.org/10.1038/ngeo2518, 2015.

Baskota, S., Khanal, G. P., Bhusal, B., Bhandari, G., and Bhattarai, N.: Investigation of Cause of Disaster and Future Risk around Melamchi-Bhemathang area, Sindhupalchok, Tech. rep., 2021.

Bookhagen, B. and Burbank, D. W.: Toward a complete Himalayan hydrological budget: Spatiotemporal distribution of snowmelt and rainfall and their impact on river discharge, Journal of Geophysical Research: Earth Surface, 115, 1–25, https://doi.org/10.1029/2009JF001426,
520 2010.

Chen, H. and Petley, D. N.: The impact of landslides and debris flows triggered by Typhoon Mindulle in Taiwan, Quarterly Journal of Engineering Geology and Hydrogeology, 38, 301–304, https://doi.org/10.1144/1470-9236/04-077, 2005.

Clubb, F. J., Mudd, S. M., Milodowski, D. T., Valters, D. A., Slater, L. J., Hurst, M. D., and Limaye, A. B.: Geomorphometric delineation of floodplains and terraces from objectively defined topographic thresholds, Earth Surface Dynamics, 5, 369–385,
525 https://doi.org/10.5194/esurf-5-369-2017, 2017.

Collins, B. D. and Jibson, R. W.: Assessment of Existing and Potential Landslide Hazards Resulting from the April 25, 2015 Gorkha, Nepal Earthquake Sequence, Tech. Rep. August, https://doi.org/10.3133/ofr20151142, 2015.

Cook, K. L., Andermann, C., Adhikari, B. R., Schmitt, C., and Marc, O.: Post-earthquake modification of 2015 Gorkha Earthquake landslides in the Bhote Koshi River valley, in: EGU General Assembly, Vienna, 2016.

530 Cook, K. L., Andermann, C., Gimbert, F., Adhikari, B. R., and Hovius, N.: Glacial lake outburst floods as drivers of fluvial erosion in the Himalaya, Science, 362, 53–57, https://doi.org/10.1126/science.aat4981, 2018.

Crameri, F.: Scientific colour maps, https://doi.org/https://doi.org/10.5281/zenodo.1243862, 2018.

Crameri, F., Shephard, G. E., and Heron, P. J.: The misuse of colour in science communication, Nature Communications, 11, 1–10, https://doi.org/10.1038/s41467-020-19160-7, 2020.

535 Croissant, T., Lague, D., Steer, P., and Davy, P.: Rapid post-seismic landslide evacuation boosted by dynamic river width, Nature Geoscience, 10, 680–684, https://doi.org/10.1038/ngeo3005, 2017.

Dadson, S. J., Hovius, N., Chen, H., Dade, W. B., Lin, J.-C., Hsu, M. L., Lin, C. W., Horng, M.-J., Chen, T. C., Milliman, J., and Stark, C. P.: Earthquake-triggered increase in sediment delivery from an active mountain belt, Geology, 32, 733–736, https://doi.org/10.1130/G20639.1, 2004.

540 Densmore, A. L. and Hovius, N.: Topographic fingerprints of bedrock landslides, Geology, 28, 371–374, https://doi.org/10.1130/0091-7613(2000)28<371:TFOBL>2.0.CO, 2000.

Department of Mines and Geology: Geological Map of Central Nepal, 2011.

Devrani, R., Singh, V., Mudd, S. M., and Sinclair, H. D.: Prediction of flash flood hazard impact from Himalayan river profiles, Geophysical Research Letters, 42, 5888–5894, https://doi.org/10.1002/2015GL063784, 2015.

545 Dhital, M. R.: Geology of the Nepal Himalaya Regional Perspective of the Classic Collided Orogen, Springer, https://doi.org/10.1007/978-3-319-02496-7, 2015.

Egholm, D. L., Knudsen, M. F., and Sandiford, M.: Lifespan of mountain ranges scaled by feedbacks between landsliding and erosion by rivers, Nature, 498, 475–478, https://doi.org/10.1038/nature12218, 2013.

Elliott, J. R., Jolivet, R., Gonzalez, P. J., Avouac, J. P., Hollingsworth, J., Searle, M. P., and Stevens, V. L.: Himalayan megathrust geometry
550 and relation to topography revealed by the Gorkha earthquake, Nature Geoscience, 9, 174–180, https://doi.org/10.1038/ngeo2623, 2016.

Fan, X., Domènech, G., Scaringi, G., Huang, R., Xu, Q., Hales, T. C., Dai, L., Yang, Q., and Francis, O.: Spatio-temporal evolution of mass wasting after the 2008 Mw 7.9 Wenchuan earthquake revealed by a detailed multi-temporal inventory, vol. 15, https://doi.org/10.1007/s10346-018-1054-5, 2018.

Francis, O., Hales, T. C., Hobley, D. E. J., Fan, X., Horton, A. J., Scaringi, G., and Huang, R.: The impact of earthquakes on orogen-scale
555 exhumation, Earth Surface Dynamics, 8, 579–593, https://doi.org/10.5194/esurf-8-579-2020, 2020.

Gailleton, B., Mudd, S. M., Clubb, F. J., Grieve, S. W., and Hurst, M. D.: Impact of Changing Concavity Indices on Channel Steepness and Divide Migration Metrics, Journal of Geophysical Research: Earth Surface, 126, https://doi.org/10.1029/2020JF006060, 2021.

Gan, B.-r., Yang, X.-g., Zhang, W., and Zhou, J.-w.: Temporal and Spatial Evolution of Vegetation Coverage in the Mianyuan River Basin Influenced by Strong Earthquake Disturbance, Scientific Reports, 9, 1–15, https://doi.org/10.1038/s41598-019-53264-5, 2019.

560 Gansser, A.: Geology of the Himalayas, Wiley-Blackwell, London, 1964.

Gasparini, N. M., Tucker, G. E., and Bras, R. L.: Network-scale dynamics of grain-size sorting: implications for downstream fining, stream-profile concavity, and drainage basin morphology, Earth Surface Processes and Landforms, 29, 401–421, https://doi.org/10.1002/esp.1031, 2004.

Gnyawali, K. and Adhikari, B. R.: Spatial Relations of Earthquake Induced Landslides Triggered by 2015 Gorkha Earthquake Mw=7.8,
565 Advancing Culture of Living with Landslides, https://doi.org/10.1007/978-3-319-53485-5, 2017a.

Gnyawali, K. R. and Adhikari, B. R.: Earthquake induced landslides triggered by 2015 Gorkha earthquake Mw 7.8, U.S. Geological Survey data release, https://doi.org/https://doi.org/10.5066/F7028Q2X, 2017b.

Hayes, G. P., Briggs, R. W., Barnhart, W. D., Yeck, W. L., McNamara, D. E., Wald, D. J., Nealy, J. L., Benz, H. M., Gold, R. D., Jaiswal, K. S., Marano, K. D., Earle, P. S., Hearne, M. G., Smoczyk, G. M., Wald, L. A., and Samsonov, S. V.: Rapid Characterization of the
570 2015 M w 7.8 Gorkha, Nepal, Earthquake Sequence and Its Seismotectonic Context, Seismological Research Letters, 86, 1557–1567, https://doi.org/10.1785/0220150145, 2015.

Hovius, N., Meunier, P., Lin, C. W., Chen, H., Chen, Y. G., Dadson, S. J., Horng, M.-J., and Lines, M.: Prolonged seismically induced erosion and the mass balance of a large earthquake, Earth and Planetary Science Letters, 304, 347–355, https://doi.org/10.1016/j.epsl.2011.02.005, 2011.

575 Howarth, J. D., Fitzsimons, S. J., Norris, R. J., and Jacobsen, G. E.: Lake sediments record cycles of sediment flux driven by large earthquakes on the Alpine fault, New Zealand, Geology, 40, 1091–1094, https://doi.org/10.1130/G33486.1, 2012.

Huang, R. and Fan, X.: The landslide story, Nature Geoscience, 6, 325–326, https://doi.org/10.1038/ngeo1806, 2013.

Kargel, J. S., Leonard, G. J., Shugar, D. H., Haritashya, U. K., Bevington, A., Fujita, K., Immerzeel, W. W., Bawden, G. W., Breashears, D. F., Donnellan, A., Fielding, E. J., Glasscoe, M. T., Green, D., Hudnut, K., Huyck, C., Khanal, N. R., Lamsal, D., McKinney, D., Pleasants, M.,

580   Sakai, A., Shea, J. M., Shrestha, A. B., Kooij, M. V. D., and Yoder, M. R.: Geomorphic and Tectonic Controls of Geohazards Induced by
        Nepal's 2015 Gorkha Earthquake, Interdisciplinary Arts and Sciences Publications, 342, https://doi.org/10.1126/science.aac8353, 2015.

Kargel, J. S., Leonard, G. J., Shugar, D. H., Haritashya, U. K., Bevington, A., Fielding, E. J., Fujita, K., Geertsema, M., Miles, E. S., Steiner,
        J., Anderson, E., Bajracharya, S., Bawden, G. W., Breashears, D. F., Byers, A., Collins, B., Dhital, M. R., Donnellan, A., Evans, T. L.,
        Geai, M. L., Glasscoe, M. T., Green, D., Gurung, D. R., Heijenk, R., Hilborn, A., Hudnut, K., Huyck, C., Immerzeel, W. W., Jiang, L.,
585   Jibson, R., Kääb, A., Khanal, N. R., Kirschbaum, D., Kraaijenbrink, P. D., Lamsal, D., Liu, S., Lv, M., McKinney, D., Nahirnick, N. K.,
        Nan, Z., Ojha, S., Olsenholler, J., Painter, T. H., Pleasants, M., Pratima, K. C., Yuan, Q. I., Raup, B. H., Regmi, D., Rounce, D. R., Sakai,
        A., Shangguan, D., Shea, J. M., Shrestha, A. B., Shukla, A., Stumm, D., Van Der Kooij, M., Voss, K., Wang, X., Weihs, B., Wolfe, D., Wu,
        L., Yao, X., Yoder, M. R., and Young, N.: Geomorphic and geologic controls of geohazards induced by Nepal's 2015 Gorkha earthquake,
        Science, 351, https://doi.org/10.1126/science.aac8353, 2016.

590   Karki, R., Talchabhadel, R., Aalto, J., and Baidya, S. K.: New climatic classification of Nepal, Theoretical and Applied Climatology, 125,
        799–808, https://doi.org/10.1007/s00704-015-1549-0, 2016.

Keefer, D. K.: The importance of earthquake-induced landslides to long-term slope erosion and slope-failure hazards in seismically active
        regions, Geomorphology and Natural Hazards, pp. 265–284, https://doi.org/10.1016/B978-0-444-82012-9.50022-0, 1994.

Khanal, N. R., Hu, J.-M., and Mool, P.: Glacial Lake Outburst Flood Risk in the Poiqu/Bhote Koshi/Sun Koshi River Basin in the Central
595   Himalayas, Mountain Research and Development, 35, 351–364, https://doi.org/10.1659/MRD-JOURNAL-D-15-00009, 2015.

Khazai, B. and Sitar, N.: Evaluation of factors controlling earthquake-induced landslides caused by Chi-Chi earthquake and comparison with
        the Northridge and Loma Prieta events, Engineering Geology, 71, 79–95, https://doi.org/10.1016/S0013-7952(03)00127-3, 2004.

Kincey, M., Rosser, N., Robinson, T. R., Densmore, A. L., Shrestha, R., Pujara, D. S., Oven, K., Williams, J. G., and Swirad, Z. M.: Evolution
        of Coseismic and Post-seismic Landsliding After the 2015 Mw 7.8 Gorkha Earthquake, Nepal, Journal of Geophysical Research: Earth
600   Surface, 126, https://doi.org/10.1029/2020JF005803, 2021.

Koi, T., Hotta, N., Ishigaki, I., Matuzaki, N., Uchiyama, Y., and Suzuki, M.: Prolonged impact of earthquake-induced
        landslides on sediment yield in a mountain watershed: The Tanzawa region, Japan, Geomorphology, 101, 692–702,
        https://doi.org/10.1016/j.geomorph.2008.03.007, 2008.

Korup, O.: Geomorphic imprint of landslides on alpine river systems, southwest New Zealand, Earth Surface Processes and Landforms, 30,
605   783–800, https://doi.org/10.1002/esp.1171, 2005.

Korup, O., McSaveney, M. J., and Davies, T. R.: Sediment generation and delivery from large historic landslides in the Southern Alps, New
        Zealand, Geomorphology, 61, 189–207, https://doi.org/10.1016/j.geomorph.2004.01.001, 2004.

Lamichhane, S., Aryal, K. R., Talchabhadel, R., Thapa, B. R., Adhikari, R., Khanal, A., Pandey, V. P., and Gautam, D.: Assessing the
        prospects of transboundary multihazard dynamics: The case of Bhotekoshi—sunkoshi watershed in Sino—Nepal border region, Sustain-
610   ability (Switzerland), 13, 1–29, https://doi.org/10.3390/su13073670, 2021.

Larsen, I. J., Montgomery, D. R., and Korup, O.: Landslide erosion controlled by hillslope material, Nature Geoscience, 3, 247–251,
        https://doi.org/10.1038/ngeo776, 2010.

Li, G., West, A. J., Densmore, A. L., Jin, Z., Parker, R. N., and Hilton, R. G.: Seismic mountain building: Landslides associated with the 2008
        Wenchuan earthquake in the context of a generalized model for earthquake volume balance, Geochemistry, Geophysics, Geosystems, 15,
615   833–844, https://doi.org/10.1002/2013GC005067, 2014.

Li, G., West, A. J., Densmore, A. L., Hammond, D. E., Jin, Z., Zhang, F., Wang, J., and Hilton, R. G.: Connectivity of earthquake-triggered landslides with the fluvial network: Implications for landslide sediment transport after the 2008 Wenchuan earthquake, Journal of Geophysical Research: Earth Surface, 44, 1–22, https://doi.org/10.1002/2015JF003718, 2016.

Li, N., Tang, C., and Yang, T.: Ten years of landslide development after the Wenchuan earthquake: a case study from Miansi town, China, Natural Hazards, 111, 2787–2808, https://doi.org/10.1007/s11069-021-05157-y, 2022.

Lin, C. W., Shieh, C. L., Yuan, B. D., Shieh, Y. C., Liu, S. H., and Lee, S. Y.: Impact of Chi-Chi earthquake on the occurrence of landslides and debris flows: Example from the Chenyulan River watershed, Nantou, Taiwan, Engineering Geology, 71, 49–61, https://doi.org/10.1016/S0013-7952(03)00125-X, 2004.

Lin, C. W., Liu, S. H., Lee, S. Y., and Liu, C. C.: Impacts of the Chi-Chi earthquake on subsequent rainfall-induced landslides in central Taiwan, Engineering Geology, 86, 87–101, https://doi.org/10.1016/j.enggeo.2006.02.010, 2006.

Lin, W. T., Chou, W. C., Lin, C. Y., Huang, P. H., and Tsai, J. S.: Study of landslides caused by the 1999 Chi-Chi earthquake, Taiwan, with multitemporal SPOT images, Canadian Journal of Remote Sensing, 33, 289–302, https://doi.org/10.5589/m07-036, 2007.

Liu, M., Chen, N., Zhang, Y., and Deng, M.: Glacial lake inventory and lake outburst flood/debris flow hazard assessment after the gorkha earthquake in the Bhote Koshi Basin, Water (Switzerland), 12, https://doi.org/10.3390/w12020464, 2020.

Maharjan, S. B., Steiner, J. F., Shrestha, A. B., Maharjan, A., Nepal, S., Shrestha, M. S., Bajracharya, B., Rasul, G., Shrestha, M., Jackson, M., and Gupta, N.: The Melamchi flood disaster: Cascading hazard and the need for multihazard risk management, Tech. rep., https://lib.icimod.org/record/35284, 2021.

Malamud, B. D., Turcotte, D. L., Guzzetti, F., and Reichenbach, P.: Landslides, earthquakes, and erosion, Earth and Planetary Science Letters, 229, 45–59, https://doi.org/10.1016/j.epsl.2004.10.018, 2004.

Marc, O., Hovius, N., Meunier, P., Uchida, T., and Hayashi, S.: Transient changes of landslide rates after earthquakes, Geology, 43, 883–886, https://doi.org/10.1130/G36961.1, 2015.

Marc, O., Hovius, N., and Meunier, P.: The mass balance of earthquakes and earthquake sequences, Geophysical Research Letters, 43, 3708–3716, https://doi.org/10.1002/2016GL068333, 2016.

Marc, O., Behling, R., Andermann, C., Turowski, J. M., Illien, L., Roessner, S., and Hovius, N.: Long-term erosion of the Nepal Himalayas by bedrock landsliding: The role of monsoons, earthquakes and giant landslides, Earth Surface Dynamics, 7, 107–128, https://doi.org/10.5194/esurf-7-107-2019, 2019.

Martha, T. R., Roy, P., Mazumdar, R., Govindharaj, K. B., and Kumar, K. V.: Spatial characteristics of landslides triggered by the 2015 Mw 7.8 (Gorkha) and Mw 7.3 (Dolakha) earthquakes in Nepal, Landslides, 14, 697–704, https://doi.org/10.1007/s10346-016-0763-x, 2017.

Mudd, S. M., Attal, M., Milodowski, D. T., Grieve, S. W., and Valters, D. A.: A statistical framework to quantify spatial variation in channel gradients using the integral method of channel profile analysis, Journal of Geophysical Research: Earth Surface, 119, 138–152, https://doi.org/10.1002/2013JF002981, 2014.

Mudd, S. M., Clubb, F. J., Grieve, S. W. D., Milodowski, D. T., Gailleton, B., Hurst, M. D., Valters, D. A., Wickert, A. D., and Hutton, E. W. H.: LSDTopoTools2, https://doi.org/https://doi.org/10.5281/zenodo.5788576, 2021.

Pain, C. and Bowler, J.: Denudation following the November 1970 earthquake at Madang, Papua New Guinea, Z. Geomorphologie, 18, 92–104, https://cir.nii.ac.jp/crid/1572261549026670848, 1973.

Pandey, V., Gautam, D., Gautam, S., Adhikari, R., Lamsal, P., Talchabhadel, R., Puri, B., Niraula, S., Karki, S., Thapa, B. R., Subedi, S. K., Adhikari, T. L., Lamichhane, S., Shah, S. K., Bastola, S., Bhattarai, P., Dahal, B. K., Acharya, I. P., Kandel, B., Sapkota, P., Yadav, S. K.,

and Hada, C.: Multi-perspective field reconnaissance after the Melamchi debris flow of June 15, 2021 in Central Nepal, Tech. Rep. July, 2021.

655 Parker, R. N., Densmore, A. L., Rosser, N. J., De Michele, M., Li, Y., Huang, R., Whadcoat, S., and Petley, D. N.: Mass wasting triggered by the 2008 Wenchuan earthquake is greater than orogenic growth, Nature Geoscience, 4, 449–452, https://doi.org/10.1038/ngeo1154, 2011.

Pearce, A. J. and Watson, A. J.: Effects of earthquake-induced landslides on sediment budget and transport over a 50-yr period, Geology, 14, 52–55, 1986.

Planet Team: Planet Application Program Interface: In Space for Life on Earth, https://api.planet.com, 2017.

660 Regmi, A. D., Dhital, M. R., Zhang, J.-q., Su, L.-j., and Chen, X.-q.: Landslide susceptibility assessment of the region affected by the 25 April 2015 Gorkha earthquake of Nepal, Journal of Mountain Science, 13, 1941–1957, https://doi.org/DOI: 10.1007/s1162 -015-3688-2, 2016.

Rest, M.: Dreaming of pipes: Kathmandu's long-delayed Melamchi Water Supply Project, Environment and Planning C: Politics and Space, 37, 1198–1216, https://doi.org/10.1177/2399654418794015, 2019.

665 Roback, K., Clark, M. K., West, A. J., Zekkos, D., Li, G., Gallen, S. F., Champlain, D., and Godt, J. W.: Map data of landslides triggered by the 25 April 2015 Mw 7.8 Gorkha, Nepal earthquake, U.S. Geological Survey data release, https://doi.org/https://doi.org/10.5066/F7DZ06F9, 2017.

Roback, K., Clark, M. K., West, A. J., Zekkos, D., Li, G., Gallen, S. F., Chamlagain, D., and Godt, J. W.: The size, distribution, and mobility of landslides caused by the 2015 Mw7.8 Gorkha earthquake, Nepal, Geomorphology, 301, 121–138,
670 https://doi.org/10.1016/j.geomorph.2017.01.030, 2018.

Robinson, T. R., Rosser, N. J., Densmore, A. L., Williams, J. G., Kincey, M. E., Benjamin, J., and Bell, H. J.: Rapid post-earthquake modelling of coseismic landslide intensity and distribution for emergency response decision support, Natural Hazards and Earth System Sciences, 17, 1521–1540, https://doi.org/10.5194/nhess-17-1521-2017, 2017.

Saba, S. B., van der Meijde, M., and van der Werff, H.: Spatiotemporal landslide detection for the 2005 Kashmir earthquake region, Geo-
675 morphology, 124, 17–25, https://doi.org/10.1016/j.geomorph.2010.07.026, 2010.

Shrestha, B. B. and Nakagawa, H.: Hazard assessment of the formation and failure of the Sunkoshi landslide dam in Nepal, Natural Hazards, 82, 2029–2049, https://doi.org/10.1007/s11069-016-2283-3, 2016.

Sims, A. J. and Rutherfurd, I. D.: Management responses to pulses of bedload sediment in rivers, Geomorphology, 294, 70–86, https://doi.org/10.1016/j.geomorph.2017.04.010, 2017.

680 Tanoli, J. I., Ningsheng, C., Regmi, A. D., and Jun, L.: Spatial distribution analysis and susceptibility mapping of landslides triggered before and after Mw7.8 Gorkha earthquake along Upper Bhote Koshi, Nepal, Arabian Journal of Geosciences, 10, https://doi.org/10.1007/s12517-017-3026-9, 2017.

Tiwari, B., Ajmera, B., and Dhital, S.: Characteristics of moderate- to large-scale landslides triggered by the Mw 7.8 2015 Gorkha earthquake and its aftershocks, Landslides, 14, 1297–1318, https://doi.org/10.1007/s10346-016-0789-0, 2017.

685 Upreti, B. N.: An overview of the stratigraphy and tectonics of the Nepal Himalaya, Journal of Asian Earth Sciences, 17, 577–606, https://doi.org/10.1016/S1367-9120(99)00047-4, 1999.

Valagussa, A., Frattini, P., Valbuzzi, E., and Crosta, G. B.: Role of landslides on the volume balance of the Nepal 2015 earthquake sequence, Scientific Reports, 11, 1–12, https://doi.org/10.1038/s41598-021-83037-y, 2021.

van der Geest, K.: Landslide Loss and Damage in Sindhupalchok District, Nepal: Comparing Income Groups with Implications for Com-
690 pensation and Relief, International Journal of Disaster Risk Science, 9, 157–166, https://doi.org/10.1007/s13753-018-0178-5, 2018.

Wang, J., Jin, Z., Hilton, R. G., Zhang, F., Densmore, A. L., Li, G., and Joshua West, A.: Controls on fluvial evacuation of sediment from earthquake-triggered landslides, Geology, 43, 115–118, https://doi.org/10.1130/G36157.1, 2015.

Wang, W., Godard, V., Liu-zeng, J., Scherler, D., Xu, C., Zhang, J., Xie, K., Bellier, O., Ansberque, C., Sigoyer, J. D., and Team, A.: Perturbation of fluvial sediment fluxes following the 2008 Wenchuan earthquake, Earth Surface Processes and Landforms, 42, 2611–
695   2622, https://doi.org/10.1002/esp.4210, 2017.

Weidinger, J. T.: Landslide dams in the high mountains of India, Nepal and China–stability and life span of their dammed lakes, Italian Journal of Engineering Geology and Environment, 1, 67–80, https://doi.org/10.4408/IJEGE.2006-01.S-08, 2006.

Whadcoat, S.: Landsliding and sediment dynamics following the 2008 Wenchuan Earthquake in the Beichuan area of China, Masters thesis, Durham University, http://etheses.dur.ac.uk/1369/, 2011.

700   Whipple, K. X., DiBiase, R. A., and Crosby, B. T.: Bedrock Rivers, in: Treatise on Geomorphology, vol. 9, pp. 550–573, Elsevier Ltd., https://doi.org/10.1016/B978-0-12-374739-6.00254-2, 2013.

Whitworth, M. R., Moore, A., Francis, M., Hubbard, S., and Manandhar, S.: Building a more resilient Nepal - The utilisation of the resilience scorecard for Kathmandu, Nepal following the Gorkha Earthquake of 2015, Lowland Technology International, 21, 229–236, https://doi.org/10.0001/ialt_lti, 2020.

705   Williams, J. G., Rosser, N. J., Kincey, M. E., Benjamin, J., Oven, K. J., Densmore, A. L., Milledge, D. G., Robinson, T. R., Jordan, C. A., and Dijkstra, T. A.: Satellite-based emergency mapping using optical imagery: Experience and reflections from the 2015 Nepal earthquakes, Natural Hazards and Earth System Sciences, 18, 185–205, https://doi.org/10.5194/nhess-18-185-2018, 2018.

Xu, C.: Landslides triggered by the 2015 Gorkha, Nepal Earthquake, International Archives of the Photogrammetry, Remote Sensing and Spatial Information Sciences - ISPRS Archives, 42, 1989–1993, https://doi.org/10.5194/isprs-archives-XLII-3-1989-2018, 2018.

710   Yanites, B. J., Tucker, G. E., Mueller, K. J., and Chen, Y. G.: How rivers react to large earthquakes: Evidence from central Taiwan, Geology, 38, 639–642, https://doi.org/10.1130/G30883.1, 2010.

Yin, A.: Cenozoic tectonic evolution of the Himalayan orogen as constrained by along-strike variation of structural geometry, exhumation history, and foreland sedimentation, Earth-Science Reviews, 76, 1–131, https://doi.org/10.1016/j.earscirev.2005.05.004, 2006.

Yin, Y., Wang, F., and Sun, P.: Landslide hazards triggered by the 2008 Wenchuan earthquake, Sichuan, China, Landslides, 6, 139–151,
715   https://doi.org/10.1007/s10346-009-0148-5, 2009.